

Research paper

Computational analysis and experiments of spatter transport in a laser powder bed fusion machine

Nicholas O'Brien^a, Syed Zia Uddin^a, Jordan Weaver^b, Jake Jones^c, Satbir Singh^{a,*}, Jack Beuth^a

^a Department of Mechanical Engineering, Carnegie Mellon University, 5000 Forbes Avenue, Pittsburgh, 15213, PA, USA

^b National Institute of Standards and Technology, Engineering Laboratory, Gaithersburg, MD, USA

^c Penn United Technologies, Inc., 799 N Pike Rd, Cabot, 16023, PA, USA

ARTICLE INFO

Keywords:

Laser powder bed fusion
Spatter particles
Computational fluid dynamics (CFD)
Discrete phase model (DPM)
Process monitoring

ABSTRACT

This work focuses on how spatter particles are transported within a laser powder bed fusion (L-PBF) machine. The machine's gas flow rate and salient flow features are studied with a computational fluid dynamics (CFD) model and are validated with experimental measurements of the flow near the build plate. The CFD model is also paired with a discrete phase model (DPM) to show how a spatter particle's diameter, speed, ejection angle, material, and ejection location each affect its trajectory. The spatter model results are also validated by experiments wherein hot spatter particles are identified with an infrared camera. Overall, this work brings focus to several spatter-mitigation strategies including increasing gas flow rate, controlling spatter production through laser settings, and changing part placement. Throughout the infrared experiment's single build cycle, over 14 million spatter particles were detected, contaminating both the parts and the powder bed. Both the spatter model and experiment suggest that spatter particles travel primarily in the downstream direction. This suggests that placing parts next to one another instead of downstream from one another could be a strategy to prevent spatter particles from traveling between parts. A low-speed zone is also discovered beneath the lower nozzle and is predicted to negatively alter the removal of spatter from that region of the build area.

1. Introduction and background

Laser powder bed fusion (L-PBF) is an additive manufacturing (AM) process that overcomes the restrictions of many traditional manufacturing processes. The process produces parts in a layerwise fashion by selectively melting a powder with a laser. Many powder materials can be used with this process, including polymers, ceramics, and metal alloys. This process uses resources more efficiently than traditional processes, partly because of the ability to reuse powder [1]. It is no wonder, then, that aerospace, medical, and defense industries are adopting L-PBF as a primary production process [2]. Despite the advantages of L-PBF, it still often fails to produce zero-defect parts for high-fatigue life applications. Porosity defects are one of the types of defects that prevent L-PBF from consistently producing parts that meet the demands for these applications.

Porosity has a deleterious effect on part performance in areas such as ductility [3–5], surface roughness [4,6,7], and high-cycle fatigue life [8–10]. According to a review paper by Mostafei et al. [9], pores arise mainly from the powder, laser settings, and scan-pattern settings. Improper laser power and speed can cause keyholing and lack-of-fusion (LOF) defects (among others), which are characterized by spherical

pores [11] and irregularly shaped pores, respectively [12]. Keyholing is generally a result of a high laser power and low scanning speed. In this regime, the laser vaporizes the material in the melt-pool, producing a vapor plume. This vapor plume is estimated to eject at a speed near tens of meters per second for SS316L [13] and up to hundreds of meters per second for Ti6Al4V [14]. The plume's high momentum applies a recoil pressure to the melt-pool, pushing the melt-pool deeper into the material and creating the “keyhole” shape. When the “keyhole” collapses, gas becomes entrapped as a pore in the solidified material.

LOF, on the other hand, occurs when the laser cannot melt sufficient material to join to the adjacent melt-tracks, leaving voids in the final part [15]. This generally occurs when the laser power is too low for its scanning speed, track spacing, and layer height. The causes of defects from process parameters are well understood in AM, but even with correct process parameters, parts will only reach 99% density [16]—this is likely because of spatter-induced porosity.

Spatter is a byproduct of the melt-pool's internal flow, the vapor plume, and the surrounding powder [13,17–19]. Ly et al. [13] found through experiments and multiphysics simulations that the two main causes of spatter are the recoil pressure on the melt-pool and the

* Corresponding author.

E-mail address: satbirs@andrew.cmu.edu (S. Singh).

entrainment of surrounding particles, the latter of which is commonly referred to as powder denudation. Spatter particles can be much larger than the base powder [4,19–21], and if a spatter particle is too large to be melted with the laser's current settings, it can cause LOF porosity or increase surface roughness [7,8,10,16,22]. These larger spatter particles are a concern throughout a build cycle, but they can be sieved out of the powder once a build cycle is finished, preventing further LOF defects from these particles.

However, even printing with the reused and sieved powder has been linked to reduced ductility in parts made from some steel alloys [4,5]. Fedina et al. [20] found that reused powder is often contaminated with spatter that is too small to be removed with a sieve. Fedina's results also show that the amount of oxygen in a set of powder increases with the number of reuses, which could be a result of the increasing amount of spatter contaminating the powder. Spatter particles have been shown to develop a surface oxide layer despite the inert gas environment in L-PBF, as shown by results in Laleh et al. [16] and Ohtsuki et al. [10]. Reusing powder contaminated with spatter could thus introduce oxygen to the melt-pool.

There are several strategies for reducing spatter contamination during a build cycle. The most direct approach is to use process parameters to control the mechanisms that generate spatter: the vapor plume and powder denudation. Several studies [13,23–26] have results which suggest that changing laser power or scan speed will affect both the quantity of ejected spatter particles and the diameters, ejection speeds, and ejection angles of said spatter particles. Computational and experimental results from Ly et al. [13] suggest that changes in laser parameters will change the speed and angle of the vapor plume, which would likewise influence the ejection speeds and angles of any entrained spatter particles. A melt-pool in the desirable process window will feature a vapor plume pointing backwards at some angle above the powder bed, but as the melt-pool approaches keyholing, the vapor depression deepens and the vapor plume becomes more vertical [27]. This vertical vapor plume would also likely cause spatter particles to be ejected vertically.

Controlling laser parameters directly could be a method to control the spatter that is produced, but this approach is unlikely to eliminate spatter contamination entirely. Flooding the build chamber with helium [28] or pressurizing the build chamber [29–31] are both approaches which seem promising to reduce the amount of entrained spatter. Presintering the powder with a fast-scanning laser has also been suggested in many instances to prevent powder denudation and entrainment. The downside with these approaches is the lack of applicability to existing machines or the increased cost associated with implementing the approach¹ [31]. The final approach that many machine manufacturers take is to manipulate the inert gas flow within the machine.

The inert gas flow aims to transport the vapor plume and spatter particles away from the melt-pool without disturbing the powder bed. Experiments from Reijonen et al. [32] showed how increasing the inert gas flow rate could reduce part porosity. This result was theorized to be a consequence of the higher flow rate removing more spatter particles from the build area. On the other hand, initial results from works like Ladewig et al. [33] mention that the gas flow does not remove enough spatter to eliminate spatter contamination. More recent works from Snow et al. [34] and Schwerz et al. [35] expand on this and show that spatter is actually just carried downstream to contaminate other regions of the build area instead of being removed from the machine entirely.

Other researchers have also conducted computational studies (e.g., [36–43]) using computational fluid dynamics (CFD) to simulate the inert gas flow within a computer model of the machine. Many of the prior works focus on changing the design of the machine to improve

¹ Helium is more expensive than argon, and presintering adds to the layer time, which thereby increases the part's cost.

the uniformity of the gas flow over the build area. Philo et al. [38], Zhang et al. [36], Chen et al. [40], and Wirth et al. [37] each note the importance of the gas nozzle's design. In particular, if the nozzle is not flush with the powder bed, the jet will create a low-pressure recirculation zone beneath itself. This low-pressure zone disallows the jet from attaching to the entire build plate via the Coanda effect [36], causing a non-uniform flow profile over the build area. This non-uniform flow can be detrimental to spatter transport because spatter particles will be transported differently depending on their ejection location.

In addition to CFD, many studies couple their flow predictions with a discrete phase model (DPM). The DPM calculates the trajectories of user-defined particles based on the CFD-model's predicted flow. Philo et al. [39], Anwar et al. [41], Zhang et al. [36], and Wirth et al. [37] each used this approach to predict the transport of spatter within the machines that they modeled. In general, they defined the distributions for a spatter's diameter, speed, and ejection angle based on experiments of their own or those from literature (for example, distributions reported in Gunenthiram et al. [24] or Ly et al. [13]). Each CFD-DPM simulation showed, to some extent, that larger particles landed closer to their ejection location than smaller particles, and faster particles traveled further than slower particles. Chien et al. [43] worked to replace the DPM with the discrete element method (DEM), which could be used to additionally model the particles in the powder bed. Their initial work did not model the powder bed as a collection of particles, but their model did give similar results to those of Anwar et al. [41].

A more recent CFD-DPM model from Altmeppen et al. [42] took a different approach from the prior works by simulating the gas flow in a transient manner with fewer modeling assumptions. Their model included effects that many of the prior works had not, such as a moving heat source, buoyancy-induced flows, and the effects of laser speed and power on spatter production. Their model seemed to predict the transport of spatter particles well for a user-specified laser path, allowing them to closely match the conditions of a build cycle/experiment.

Each of the prior works have studied spatter particles, but no single study has displayed how all different aspects of a spatter particle's characteristics will affect its flight. For example, Wirth et al. [37] examines how spatter diameter and ejection velocity will affect a particle's trajectory, but they only eject spatter particles in one direction at one location on the build area. Contrast this with studies from Altmeppen et al. [42] and Zhang et al. [36], which do eject particles in other directions, but they do not discuss how the printing location on the build area may affect spatter particle transport. Furthermore, none of the prior works have examined how the material of a spatter particle may impact its trajectory, which could have a significant impact given the wide range of densities in AM materials. The current work aims to address these gaps in literature and contribute to the existing understanding of spatter transport by examining how a spatter particle's diameter, ejection velocity, ejection direction, ejection position on the build area, and material density affect its trajectory.

The current work is carried out using a CFD-DPM model of the EOS M290 L-PBF machine,² which, to the authors' knowledge, no prior computational works have investigated. This machine's flow design is also typical of most L-PBF machines, so findings from this work will likely be transferable to different machines. The computational model from the current work is validated by experimental measurements of both the inert gas flow and spatter transport.

The current work uses these experiments and models to investigate three topics: (1) how the flow develops within the EOS M290, and

² Certain commercial equipment, instruments, or materials are identified in this paper in order to specify the experimental procedure adequately. Such identification is not intended to imply recommendation or endorsement by NIST, nor is it intended to imply that the materials or equipment identified are necessarily the best available for the purpose.

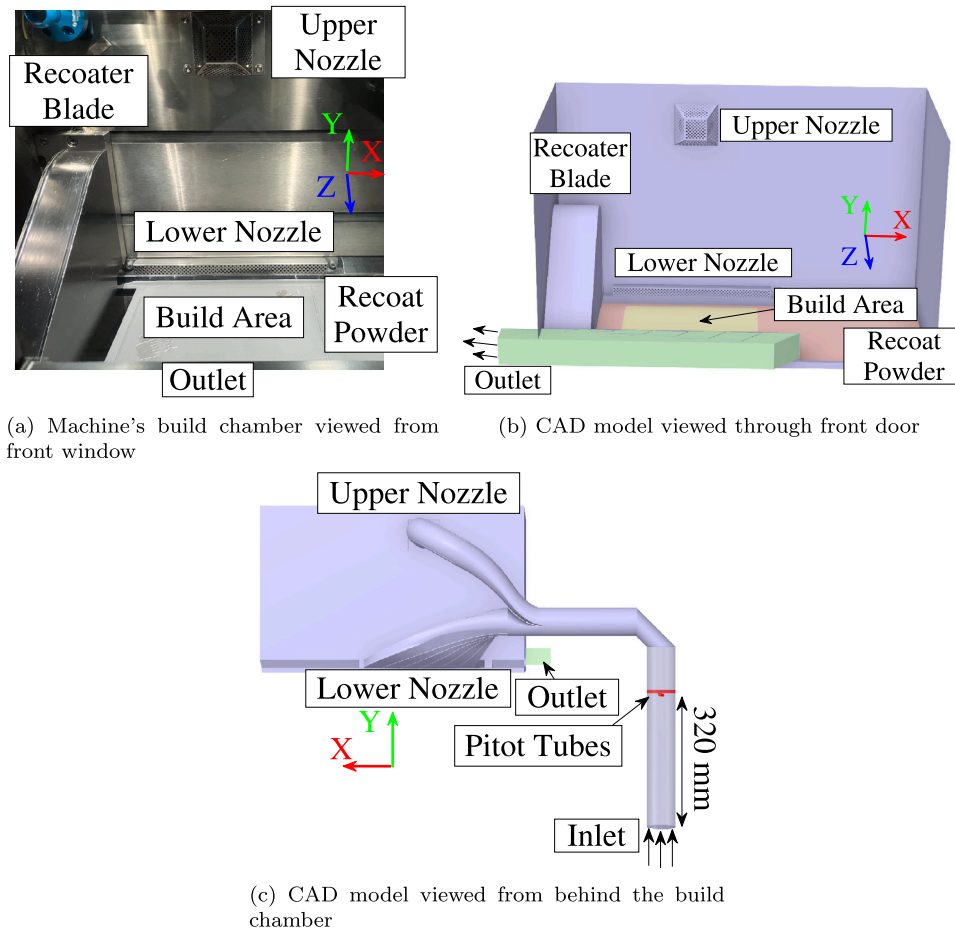


Fig. 1. Pictures of the EOS M290 machine and the corresponding CAD model of it.

which design choices seem to alter the flow; (2) how a spatter particle's diameter, ejection speed, ejection angle, material density, and ejection location each affect its movement within the build chamber; and (3) how the gas flow rate of the machine affects spatter transport.

2. Computational methods

The model presented in this work relies on two sub-models: a flow model and a spatter model. The flow model uses computational fluid dynamics (CFD) in ANSYS Fluent 2021 R2 to predict the velocity, pressure, and turbulence of the inert gas flow in the EOS M290 machine. The flow model is one-way-coupled with the spatter model, which uses ANSYS Fluent's discrete phase model (DPM) to predict the transport of ejected spatter particles.

2.1. Computational domain

The EOS M290, shown in Fig. 1(a), features an upper and a lower nozzle, both of which supply gas to the build chamber. The upper nozzle is thought to prevent recirculation of byproducts in the build chamber [37,44]. The lower nozzle is thought to be responsible for removing the vapor plume and spatter from the melt pool [32,33]. The nozzles are both centered above the build area, which is a square measuring 250 mm by 250 mm. The gas flow exits the machine at the outlet on the other end of the build area.

A computer-aided design (CAD) model was developed from pictures and measurements of the machine. The computer model includes the geometry of the build chamber (best seen in Fig. 1(b)), the nozzles, the outlet, the recoater blade, the powder bed, the build area, and the

tubing behind the build chamber (best seen in Fig. 1(c)). The tubing behind the machine connects the upper and lower nozzles to a single inlet, which is connected to a blower pump that is external to the machine. The blower pump is not included in the CAD model.

The model is meshed with about 15 million cells. Hexahedral cells were used in the build chamber, tubing, and outlet where possible. Tetrahedral cells were placed in other areas, and pyramidal cells were used between these regions to keep the mesh conformal. An inflation mesh is applied to the build area, chamber walls, outlet, and nozzles where possible capture turbulence effects.

2.2. Flow model

The flow model calculates a numerical solution to the incompressible³ steady-state⁴ Reynolds Averaged Navier–Stokes (RANS) equations for momentum and mass conservation:

$$\rho_f \nabla \cdot (\mathbf{u}_f) = 0 \quad (1)$$

$$\rho_f \nabla \cdot (\mathbf{u}_f \otimes \mathbf{u}_f) = -\nabla P - \nabla \cdot (\boldsymbol{\tau}^{(v)} + \boldsymbol{\tau}^{(l)}) + \rho_f \mathbf{g} \quad (2)$$

t is time; $\nabla = [\frac{\partial}{\partial x}, \frac{\partial}{\partial y}, \frac{\partial}{\partial z}]$ is the gradient operator with respect to the cartesian coordinates x , y , and z ; \mathbf{u}_f is the fluid velocity vector; P is static pressure; $\boldsymbol{\tau}^{(v)}$ is the viscous stress tensor, which is proportional

³ This is a reasonable assumption so long as no fluid speed surpasses a Mach number of 0.1 [45, Chapter 1] (32.3 m/s in argon).

⁴ The machine flow must reach steady-state before printing can begin.

to the dynamic viscosity of the fluid; $\tau^{(t)}$ is the Reynolds Stress tensor, which is calculated by the turbulence model; g is the acceleration due to gravity. Note that the variables of interest, u_f and P , are their ensemble-averaged quantities even though the overbar is omitted.

Turbulence effects are modeled with the Shear-Stress Transport (SST) $k-\omega$ model, based on recommendations from the Fluent User Guide [46, Chapter 13]. This model is meant to act as a versatile turbulence model for near-wall and far-field performance. k is the turbulent kinetic energy and ω is the specific dissipation rate of that energy. These quantities are transported via the following equations:

$$\rho_f \nabla \cdot (k u_f) = \nabla \cdot (\Gamma_k \nabla k) + \tilde{G}_k - Y_k \quad (3)$$

$$\rho_f \nabla \cdot (\omega u_f) = \nabla \cdot (\Gamma_\omega \nabla \omega) + G_\omega - Y_\omega + D_\omega \quad (4)$$

Γ_k and Γ_ω are the diffusivities of k and ω , respectively; G_k and G_ω represent the generation terms for k and ω , respectively; Y_k and Y_ω represent the dissipation terms of k and ω , respectively; D_ω represents the cross-diffusion term, which blends the effects of the standard $k-\epsilon$ model and the standard $k-\omega$ model, improving performance away from walls. More information regarding the turbulence model can be found in the ANSYS Fluent Theory Guide [45, Chapter 4].

Eqs. (1), (2), (3), and (4) are solved numerically with Fluent's Pressure-based Coupled solver. Second-order-accurate upwind schemes are used for first-derivative terms, and a second-order-accurate central differencing scheme is used for all second-derivative terms.

2.2.1. Boundary conditions

A velocity boundary condition is applied perpendicular to the inlet cross-section (visible in Fig. 1(c)), and a 0 Pa gauge pressure is applied to the outlet (visible in Fig. 1(b)). All walls are treated with the no-slip condition, such that velocity at those boundaries is zero. Gravity acts in the negative y -direction with a magnitude of 9.81 m/s^2 . Turbulence at the model's inlet is prescribed with turbulent intensity, I , according to the following equation from the ANSYS Fluent User's Guide [46, Chapter 7]:

$$I = 0.16 Re^{-1/8} \text{ where } Re = \frac{\rho_f D_h |u_{f,inlet}|}{\mu} \quad (5)$$

D_h is the hydraulic diameter of the inlet: 66.6 mm. At the no-slip walls in the model, the turbulence model prescribes values of k and ω depending on y^+ , the non-dimensional height of the cell adjacent to that wall. y^+ is used in turbulence modeling to calculate boundary conditions at walls in the computational mesh. It is defined as the following:

$$y^+ = \frac{\rho_f u_\tau y}{\mu}, \text{ where } u_\tau = \sqrt{\frac{\tau_w}{\rho_f}} \quad (6)$$

ρ_f is the fluid density; u_τ is the friction velocity at the wall; y is the dimensional distance from the wall; μ is the dynamic viscosity of the fluid, τ_w is the shear stress magnitude at the wall.

The SST $k-\omega$ turbulence model calculates values for k and ω at walls in the model according to wall-functions that are considered y^+ insensitive, which make them applicable for $y^+ \lesssim 300$ [45, Chapter 4]. The computational mesh in this work achieves a maximum y^+ of 38 when the model's inlet velocity is 20 m/s, meaning all cells will be well within the applicable range of the turbulence model for the flow rates tested in the current work. The equations for these functions are omitted for sake of space, but they can be found in the ANSYS Fluent Theory Guide [45, Chapter 4].

Finally, the current work presents results for the two gases that the EOS M290 can accept: pure nitrogen and pure argon. Table 1 shows the relevant material properties for each gas in the model. Results shown in Sections 4.1 and 4.2 are generated with nitrogen gas; all other results use argon.

Table 1
Material Parameters.

Material	Density kg/m ³	Viscosity kg/(m s)
Argon [46,47]	1.62	2.13×10^{-5}
Nitrogen [46,47]	1.14	1.66×10^{-5}
AlSi10Mg [48]	2,670	–
Ti-6Al-4V [49]	4,430	–
Inconel 718 [50]	8,170	–
Woka 3502 [51]	13,800	–

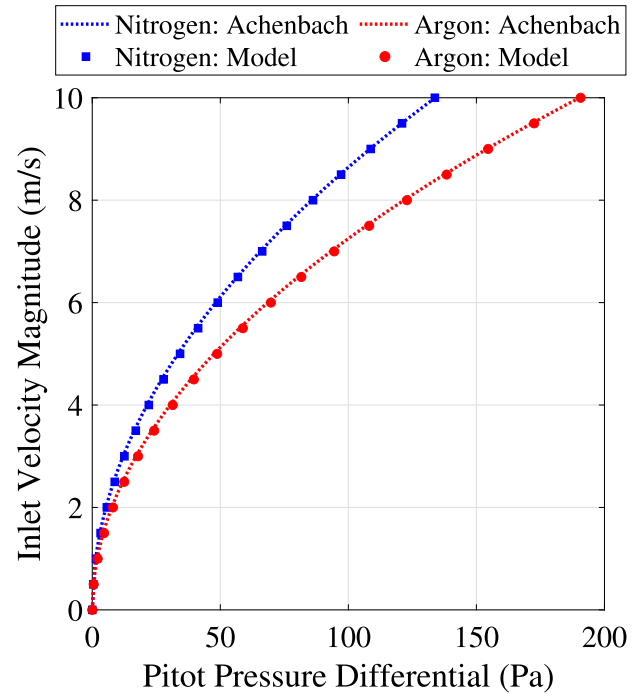


Fig. 2. Relationship between typical machine setting (pressure) and CFD model setting (inlet velocity magnitude). The lines represent the empirical correlation predicted by measurements from Achenbach [52]. Squares/circles on the graph indicate the pitot pressures measured within the flow model.

2.2.2. Flow model setting vs. machine setting

The velocity magnitude at the inlet must be linked to the machine's pressure setting. The machine's pressure setting is the relative pressure between two pitot tubes: ΔP . The pitot tubes are located in the machine's inlet tubing; this is about 320 mm downstream from the model's inlet (see Fig. 1(c)). The pitot tubes are oriented such that one tube faces towards the flow and the other tube faces away from it; essentially, one pitot tube measures the stagnation pressure, and the other measures the pressure of its wake. According to experiments from Achenbach [52], the pressure in the front of a cylinder in cross-flow should remain constant with the Reynolds number of the fluid. Conversely, the pressure at the rear of the cylinder should change with the Reynolds number. This means that the difference in pressure between the pitot tubes will vary with the Reynolds number, and hence the pressure differential, ΔP , will be related to flow speed at the inlet of the machine [52–54].

Results from Achenbach [52] give the local pressure at the front and rear of a cylinder for a variety of flows. Achenbach's results report a nondimensional pressure coefficient, C_i , which is defined as follows:

$$C_i = \frac{P_i - P_\infty}{\frac{1}{2} \rho_f |u_{f,inlet}|^2} \quad (7)$$

where P_i is the local pressure on the cylinder's surface (what the pitot tube would measure), and P_∞ is the pressure of the fluid far away from

the cylinder. The pressure differential can be written in terms of the pressure coefficients according to Eq. (7) in such a way that P_∞ does not need to be known:

$$\Delta P = P_1 - P_2 = \frac{1}{2} \rho_f |u_{f,inlet}|^2 (C_1 - C_2) \quad (8)$$

where the subscript 1 refers to the value at the front of the tube and the subscript 2 refers to the value at the back of the tube. These values would correspond to the pressure in the flow-facing tube and the wake-facing tube in the machine, respectively.

The pitot tubes have a diameter of about 7.62 mm, so for most flow speeds of the machine, the Reynolds number will be below 1×10^5 . From Achenbach [52], the pressure coefficients at a Reynolds number of 1×10^5 are $C_1 = 1$ and $C_2 = -1.35$. These pressure coefficients are used to calculate the differential pressure predicted by Eq. (8) for an inlet velocity ranging from 0 m/s to 10 m/s, as shown in Fig. 2.

In the flow model, the pressure differential is retrieved directly from its pitot tubes. The pressure differential from the flow model is calculated for inlet velocities from 0 m/s to 10 m/s and is plotted in Fig. 2.

Fig. 2 demonstrates several important features of the gas flow: (1) the flow model's inlet velocity magnitude is very close to what would be predicted by Achenbach's results [52], (2) the EOS M290's machine setting is not linearly related to the flow-speed in the machine, and (3) the type of gas used changes the flow speed for a given machine setting. The similarity between the model and Achenbach's results [52] suggests that the correct inlet velocity is being applied to the flow model.

2.3. Spatter model

The spatter model calculates the trajectories of ejected spatter particles. The ejected particles' trajectories are theoretically governed by the forces that change their momenta, which is described by the following system of differential equations [45, Chapter 12]:

$$\frac{\pi}{6} \rho_p D_p^3 \frac{\partial \mathbf{u}_p}{\partial t} = \mathbf{F}_G + \mathbf{F}_D \quad (9)$$

$$\frac{\partial \mathbf{x}_p}{\partial t} = \mathbf{u}_p \quad (10)$$

ρ_p is the density of the particle's material; D_p is the diameter of the particle; \mathbf{u}_p is the particle velocity; t is time; \mathbf{F}_G is the combined force of gravity and buoyancy acting on the particle; \mathbf{F}_D is the drag force acting on the particle; \mathbf{x}_p is the particle's position vector. Spatter particles are assumed spherical, so the drag and gravity forces are defined as follows [45, Chapter 12]:

$$\mathbf{F}_G = \frac{\pi}{6} D_p^3 (\rho_p - \rho_f) \mathbf{g} \quad (11)$$

$$\mathbf{F}_D = \frac{\pi \mu D_p}{8} C_D Re_D (\mathbf{u}_f - \mathbf{u}_p) \quad \text{where} \quad Re_D = \frac{\rho_f D_p |\mathbf{u}_f - \mathbf{u}_p|}{\mu} \quad (12)$$

μ is the dynamic viscosity of the fluid; C_D is the drag coefficient calculated according to the particle's Reynolds number, Re_D . ANSYS Fluent calculates the drag coefficient according to an equation reported by Morsi and Alexander [55]⁵:

$$C_D = \frac{a_1}{Re_D} + \frac{a_2}{Re_D^2} + a_3 \quad (13)$$

The coefficients a_1 , a_2 , and a_3 are reported in Morsi and Alexander [55], and they change depending on the Reynolds number of the particle.

⁵ A study from Barati et al. [56] shows that Morsi and Alexander's correlation is among the most accurate and is only surpassed by a machine-learning approach and a correlation from Cheng [57]. According to this study, the correlation from Haider and Levenspiel [58] yields drag coefficients of a similar accuracy to Morsi and Alexander [55].

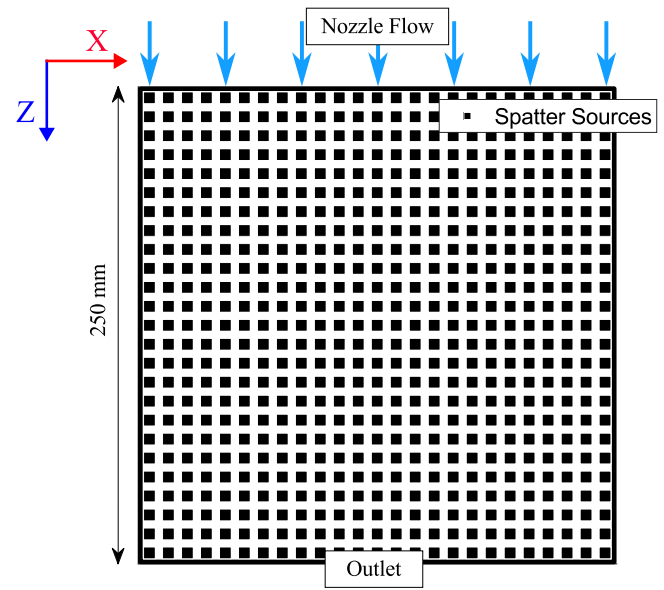


Fig. 3. 25 × 25 grid of spatter sources for parameter investigation. The black borders indicate the extent of the build area.

Eqs. (9) and (10) are numerically integrated in time with either a high-order scheme or a low-order scheme. The high-order scheme is automatically chosen when the particle travels through regions where the drag force changes quickly and a higher degree of accuracy is necessary. In regions where the drag force is less dynamic, the more stable low-order scheme is chosen to allow for a larger time-step size. This work uses the trapezoidal scheme for the high-order and the implicit Euler scheme for the low-order, as they are described in the ANSYS Fluent Theory Guide [45, Chapter 12].

The integration time step is calculated within Fluent such that the particle will have at least five integration steps before it leaves a computational cell in the mesh. Fluent will refine the time-step further until the relative change of the particle's values is less than a tolerance of 1×10^{-5} . Every particle is given a maximum of 50,000 time steps to reach one of two possible end conditions: exit through the outlet of the machine or land on the powder bed. After reaching an end condition, the particle is removed from the model. Particles collide perfectly elastically with other surfaces of the machine, do not collide with one another during flight, and do not alter the flow variables of the gas during their flight because the flow and spatter models are coupled one-way.

2.3.1. Spatter initial conditions and parameters

For the sake of building the spatter model, this model simplifies the process through which spatter is ejected. In the model, spatter particles are ejected from point sources on the build area instead of from a melt-pool/vapor plume. Works like Yin et al. [59] have shown how the vapor plume can affect the initial trajectories of spatter particles. The current work injects spatter particles with diameters, velocities, and directions that are chosen based on experiments from literature, which would include the local effects from the melt-pool and plume.

The position of a point source is the initial position of any particle ejected from that source. This study places sources in two configurations: (1) a 25 × 25 grid, shown in Fig. 3, and (2) a grid of square parts, as shown in Fig. 4. A spatter particle's diameter, speed, elevation angle, and azimuth angle are each defined by distributions; these distributions are identical for each spatter source.

Spatter particles are ejected with a random azimuth and elevation angle. The azimuth angle of the velocity is measured relative to the flow direction (Z-axis), and the elevation angle is the velocity's angle above

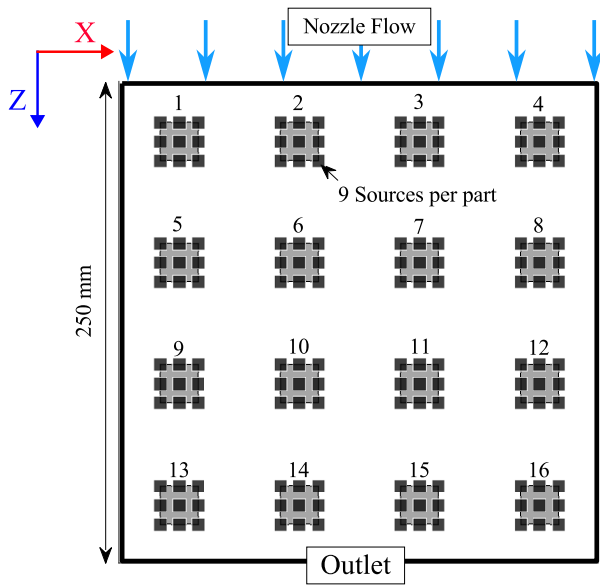


Fig. 4. Placement of square parts on EOS M290 Build Plate for Experiment. The source placement for the corresponding setup in the spatter model are shown as black squares over the parts. Numbers indicate exposure order for experiment. The black borders indicate the extent of the build area.

the powder bed (XZ-plane). For example, a particle with an azimuth angle of 0° is oriented towards the outlet and an azimuth angle of 180° is towards the lower nozzle. The distribution of azimuth angles is defined as uniform from 0° to 360°. The azimuth angle is defined as uniform in all directions to mimic the effect of rotating the scan-direction by 67° each layer, which is a common setting on the EOS M290. While spatter normally comes from the back or front of the melt-pool for a single scan-line, the melt-pool will have traveled in many directions over the course of several layers, thus ejecting spatter in every direction a uniform amount.

An elevation angle of 90° would be straight upwards (the model's positive Y-direction). The distribution of elevation angles is defined as uniform from 5° to 85°. The elevation angle range is chosen based on the figures demonstrating vapor plume angles shown in several sources [13,14,23,60].

The diameters and speeds of ejected spatter particles are also varied. It is likely that speed and diameter are correlated, but their exact relationship is yet to be revealed. From Gunenthiram et al. [24], it is suggested that larger spatter particles (e.g., 100 μm) are ejected at lower speeds than smaller spatter particles (e.g., 50 μm). This study chooses to eject spatter at 25 discrete diameter-speed pairs. The diameters and speeds chosen are shown in Table 2. There are 1000 spatter particles ejected for each speed-diameter pair, so each spatter source ejects 25,000 spatter particles. The number 1000 is chosen to eject enough particles to completely cover the ejection angle distributions.

The spatter ejected from all point sources is defined with the density of Inconel 718, which is listed in Table 1. For the sake of demonstrating the effect of particle density on spatter transport, spatter particles are also defined as other materials only in Fig. 8(c) (in Section 4.4). These other materials are AlSi10Mg, Ti-6Al-4V, and Woka 3502,⁶ and their properties are also listed in Table 1. These materials are not meant to be an exhaustive study of all AM materials. Furthermore, while it is likely true that the material choice in an experiment would affect

⁶ Woka 3502 is a tungsten carbide material with nickel added as a binding metal.

Table 2

Number of spatter particles ejected for each diameter and speed that was used in the spatter model.

Speed/Diameter	25 μm	50 μm	75 μm	100 μm	150 μm	200 μm	Total
0.1 m/s	0	0	1,000	1,000	1,000	1,000	4,000
0.5 m/s	1,000	1,000	1,000	1,000	1,000	1,000	6,000
1.0 m/s	1,000	1,000	1,000	1,000	1,000	1,000	6,000
5.0 m/s	1,000	1,000	1,000	0	0	0	3,000
10.0 m/s	1,000	1,000	1,000	0	0	0	3,000
20.0 m/s	1,000	1,000	1,000	0	0	0	3,000
Total	5,000	5,000	6,000	3,000	3,000	3,000	25,000

process parameters and the sizes and speeds of spatter produced,⁷ the same spatter particles are ejected for each material in the current work.

2.3.2. Spatter temperature prediction

Spatter temperature is not a major focus of this study, but it becomes important when investigating the results from the spatter experiment. In that case, the spatter model includes an additional equation to calculate the heat balance between the particle and its surroundings. The exchange of heat between the particle and the surrounding fluid is governed by the following equation, which assumes that temperature is uniform throughout the particle [45, Chapter 12]:

$$\rho_p c_p V_p \frac{dT_p}{dt} = h A_p (T_f - T_p) \tag{14}$$

c_p is the specific heat of the particle; t is time; h is the convective heat transfer coefficient; A_p is the surface area of the particle; T_f is the temperature of the fluid at the particle's position. The temperature of the fluid at the inlet and the walls is set to 300 K in this case, so the temperature of the fluid is 300 K throughout the machine. The convective heat transfer coefficient of the particle is calculated by ANSYS Fluent using a Nusselt number correlation from Ranz and Marshall [45,61,62]:

$$Nu = \frac{h D_p}{k_\infty} = 2.0 + 0.6 Re_D^{1/2} \left(\frac{c_p \mu}{k_\infty} \right)^{1/3} \tag{15}$$

k_∞ is the conductivity of the gas, which is assumed to be argon with a value of 0.016 W/(m K) [46,47]. Re_D is the particle Reynolds number, as defined in Eq. (12). Eq. (14) is numerically integrated according to the same procedure described for Eqs. (9) and (10). Eq. (14) additionally requires an initial temperature to initiate the algorithm; this is assumed to be the fully-liquid melting temperature of Inconel 718 at 1,673 K [50]. The specific heat capacity of Inconel 718 is also assumed to be 435 J/(kg K) [50]. Particle temperature, as described by Eq. (14), is not investigated for the other materials discussed in this work.

3. Experimental methods

Measurements from Weaver et al. [44,63] are compared with the flow model (described in Section 2.2). Infrared (IR) imaging is used to detect hot spatter particles on the powder bed throughout a build cycle, which gives data for comparison with the spatter model (described in Section 2.3). These experimental methods are described in the following sections.

⁷ For instance, Ly et al. [13] and Young et al. [18] tested SS316L and AlSi10Mg, respectively. The way they report their results is different, but it seems that Ly reports higher speeds than Young's measurements. This is possibly a difference of the material systems they tested. Both materials also have different ranges of typical process parameters.

Table 3
Laser power and velocity settings (informed by Scime & Beuth [64]).

Number of Layers	Power (W)	Speed (mm/s)	Regime
150	285	960	Nominal
25	200	670	Desirable
25	100	336	Desirable
25	285	670	Desirable
25	285	336	Keyholing
25	200	336	Keyholing
25	250	250	Keyholing
25	300	250	Keyholing
25	100	960	lack-of-fusion

3.1. Flow experiment

Weaver et al. [44] used a hot wire anemometer to measure the flow speed at 30 locations across the build plate. At each location, they measured the speed at 10 points along the height of the lower nozzle from 4 mm to 46 mm above the build plate. The build plate was set to the appropriate height and no powder was used in the machine. Nitrogen gas at a flow setting of 58 Pa (6.6 m/s) was used. Weaver's method was limited to only measuring the combined speed generated by the Y- and Z-components of the gas velocity, u_Y and u_Z , respectively. Thus, for this comparison, the flow model's predictions are combined in a similar manner with the following equation:

$$u_{CFD} = \sqrt{u_Y^2 + u_Z^2} \quad (16)$$

3.2. Spatter experiment

Sixteen 20 mm × 20 mm × 20 mm cubes were arranged in a grid, shown in Fig. 4. They were printed with Inconel 718 using argon gas at a flow setting of 81 Pa (6.5 m/s). These cubes were printed using nine different laser power-velocity combinations, which are listed in Table 3. The process-map regimes were identified using charts from Scime & Beuth [64].

The build cycle was continuously monitored with a FLIR A655sc IR camera at a frame rate of 50 frames per second. It measured all incident radiation between the wavelengths of 3 μm and 12 μm. This radiation comes from the parts, powder bed, and spatter particles. A viewing window made from Zinc-Selenide glass is placed between the camera and the build chamber; this is necessary to block the EOS M290 laser's specific wavelength of radiation (1.07 μm) in order to protect the camera and any people outside of the machine.

The camera's pixel size projected onto the build plate was 168 μm. Although the camera can detect particles smaller than 168 μm, there is not yet a correlation to determine the size of those particles with certainty. Particles detected by the IR camera in Uddin's dissertation [65] ranged in size from approximately 200 μm to 2,000 μm. The shape of distribution of particle size was similar to size distributions shown in Gasper et al. [22], even though the sizes were very different. This infrared method has not yet been validated for measuring the sizes of detected spatter particles. Because not many spatter particles have been reported to have a size above 500 μm in literature, it is likely that some other physical phenomenon is causing spatter particles to appear larger through the IR camera than they actually are.

Temperature measurement from the IR camera is unreliable due to the variable emissivity of each item in the view of the camera; therefore, the IR camera is not used to directly quantify temperature. Instead, the camera is used to produce images, through which hot (emissive) spatter particles can be detected on the powder bed. The algorithm starts by processing each frame of the IR video with FLIR's proprietary Digital Detail Enhancement (DDE) algorithm [66] using a detail level of 5 out of 7. The DDE algorithm accentuates spatter landing locations, making them appear with more intensity in the image.

Next, the frames are processed with a color thresholding algorithm. This algorithm identifies pixels with a high intensity (specifically red/orange on a blue-green-red colorscale), which is assumed to correlate to a spatter particle. Because the internal regions of parts are also hot with a high intensity, the part contours must be excluded from the image to avoid false positives. This makes spatter particles undetectable on parts in the algorithm. Once the pixels with high intensities have been identified, a blob-detector is used to record the size (in pixels) and location of each blob, which are all assumed to be spatter particles. Subsequent frames are compared with one another to ensure that spatter is counted only when it first appears in the sequence of frames. More details on this spatter detection algorithm can be found in Uddin's dissertation in Chapter 5 [65].

4. Results and discussion

4.1. Flow measurements and comparison with flow model

The flow model's estimates of velocity compare well with experimental measurements from Weaver et al. [44,63], as seen in Fig. 5. In position A on the build area, the maximum speed occurs near 22 mm for both the CFD model and the experiment. The peak velocity for the CFD model is about 0.2 m/s slower than the experiment's measurement, but the model's speeds approach the experiments' speeds in the downstream positions.

In positions B and C, the maximum velocity shifts downwards to 18 mm and 12 mm, respectively. At position C, there is a difference between the model and the measurement near the build plate. The measurement at this position could be an outlier in the measurement data, for the flow velocity should decrease monotonically as it approaches a wall. Positions D and E show similar flow profiles to one another, which suggests that the flow does not change significantly over this region of the build area. Finally, position F reflects how the jet's peak instead begins to move upwards as it approaches the outlet.

The similarity between the flow model and the flow measurements suggests that the flow model is accurately representing the geometry and boundary conditions of the machine. The flow model used the same machine setting as was used in the experiments from Weaver et al. [44]. The velocity, shape, and development of the jet all agree well with the flow measurements across the build area. Because the spatter model predicts spatter trajectories using the velocities from the flow model, the spatter model will also predict the interactions between the gas and spatter particles reasonably well.

4.2. Overview of salient flow features

The flow model shows that the upper and lower nozzles supply about two-thirds and one-third of the total inert gas flow to the build chamber, respectively. This finding is in agreement with experimental results from Elkins et al. [67]. The flows from the upper and lower nozzle jets interact, which can be seen in the velocity contours and vectors from the flow model in Fig. 6(a). The flow from the upper nozzle is generally oriented towards the outlet (situated in the front door of the machine) and would likely be strong enough to push any spatter particles away from the laser lens at the top of the machine. The flow from the lower nozzle is also directed towards the front of the machine and is mostly parallel to the build area.

Between the two jets, there is a large space occupied by a relatively slow, large vortex. This vortex develops as a result of the two jets as they transfer momentum to the surrounding ambient gas. The lower nozzle jet and the upper nozzle jet pull ambient gas downwards and upwards, respectively. Without the upper nozzle, the lower nozzle would likely generate a counter-clockwise vortex, but the relative strength of the upper nozzle's flow results in the large clockwise vortex near the middle of the machine. This clockwise vortex would likely be beneficial for spatter particles that can reach it; most of its flow is oriented

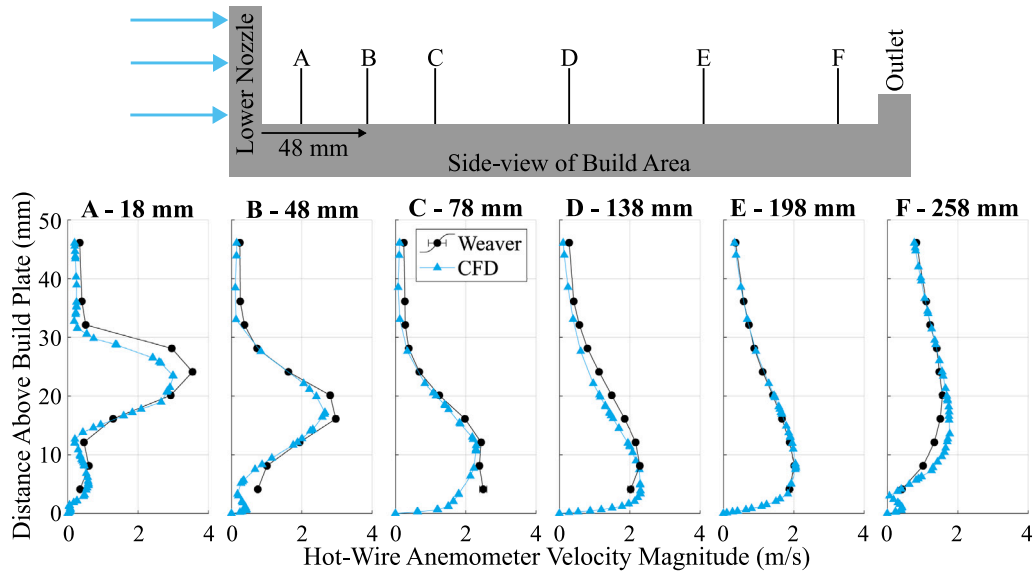
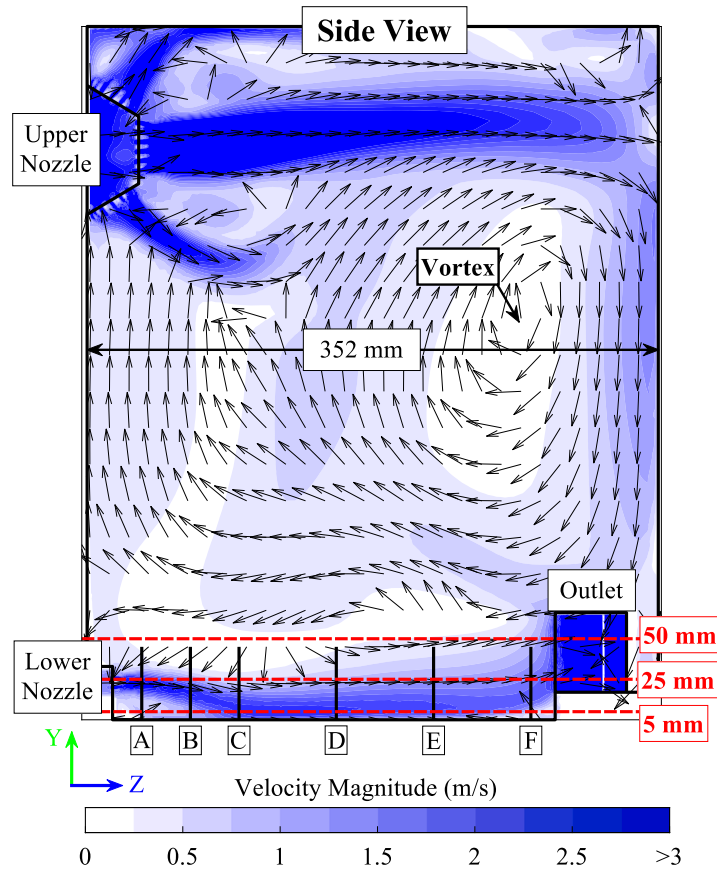
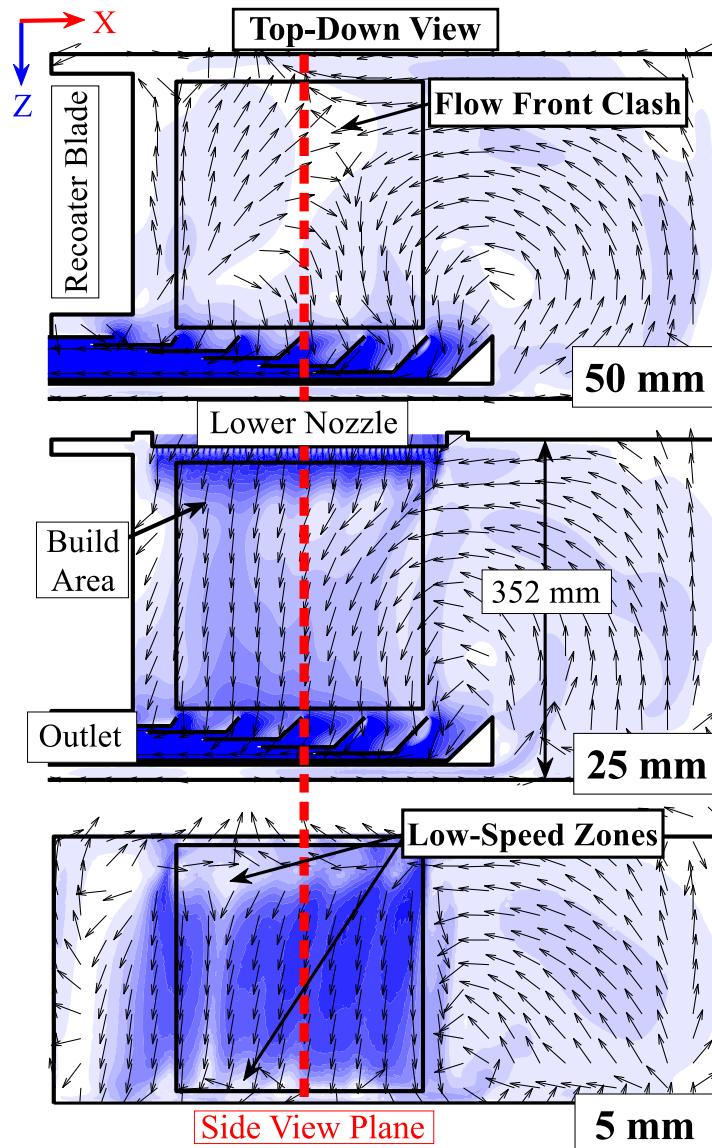


Fig. 5. Comparison between CFD from this work and flow measurements from Weaver et al. [44,63]. Locations A, B, C, D, E, and F refer to the measurement locations in the above diagram. These locations are also labeled in Fig. 6(a).



(a) Side view of build chamber at centerline of the upper and lower nozzles. The lines labeled A, B, C, D, E, and F refer to the line plots shown in Figure 5. The thick dashed lines labeled “50 mm”, “25 mm”, and “5 mm” are the heights of the contours in Figure 6b.

Fig. 6. Flow Model: Contours and vector fields of velocity at select planar slices.



(b) Top-down view of build chamber at several heights above the build area. The thick dashed line labeled “Side View Plane” indicates the position of the contours shown in Figure 6a.

Fig. 6. (continued).

upwards, which would assist particles to stay airborne rather than land on the build area. However, the vortex will likely not affect all particles; particles ejected with a slower velocity in the vertical direction may not reach this height in the machine, but all spatter particles will be affected by the performance of the lower nozzle jet in some capacity.

Fig. 6(b) shows how the lower nozzle jet velocity changes as a function of height above the build plate. The flow at 5 mm above the build plate, which a majority of spatter particles will experience, is mostly uniform except for two low-speed zones and some regions where the flow velocity points towards the lower nozzle. The low-speed zones are regions where the drag force on a particle will be very low. These low-speed zones will also not remove the vapor plume as effectively, resulting in laser attenuation [68,69]. The low-speed zone near the lower nozzle covers the first 50 mm of the build area and is predicted to be the largest near the upper left-hand corner of the build area. The low-speed zone near the outlet covers the width of the build area as well, but the effects of this zone on spatter particle transport may not be as significant because it is near the outlet.

The contour 25 mm above the build area shows a region where the flow speed is more uniform, so most particles will experience the same drag force no matter where they are above the build area. One beneficial feature of note is how the flow from the right side of the build chamber, above the recoat powder, is oriented towards the build area. This may suggest that particles will be less likely to land in the recoat powder. Finally, the flow speed at 50 mm above the build area shows the transition region where two flow fronts interact, labeled as “Flow Front Clash” in Fig. 6(b). In this view, there is a region where the flow from the left and right sides of the build chamber clash, forming a stripe that travels down the upper right-hand side of the build area. This flow feature is likely to transport some types of spatter to this region, as will be discussed in Section 4.3.

The flow contours in Fig. 6(b) show how the lower nozzle jet develops to form changing flow conditions across the build area. This changing flow across the build area is also visible in the measurements in Fig. 5. The change in flow conditions across the build area can be attributed to three factors: (1) the entrainment of the slower ambient gas in the build chamber, (2) the Coanda effect, and (3) the friction

between the fluid and the build plate. As the jet enters the build chamber, it has a high velocity compared to the surrounding ambient gas. This difference in velocity forces the jet to transfer some of its momentum to the surrounding gas, thereby widening and slowing itself.

The Coanda effect, first discussed in Zhang et al. [36], is the tendency of a jet-stream to follow the contours of a surface. In the context of this machine, the Coanda effect is what forces the lower nozzle jet to attach itself to the build plate in positions A through C, despite the initial distance between the lower nozzle and the build plate. Once the jet attaches to the build plate via the Coanda effect, the friction between the build plate and the jet slows the gas as it travels towards the outlet, which achieves the profiles seen in positions D and E. This change in flow conditions across the build area is not ideal because this means that spatter particles may not be transported as far as they could be if they are ejected underneath the low speed zones near positions A or B.

4.3. Spatter experiment and corresponding model predictions

The IR camera detected about 14 million particles throughout the 350 layers of the experiment. To best show which areas were contaminated by spatter throughout the build cycle, this work plots normalized spatter concentration. Spatter concentration is calculated by separating the build area into a uniform grid of 10,000 square bins (2.5 mm side length). If a spatter particle lands in a bin, it adds 1 to that bin's count. The final spatter concentration is normalized by the bin with the largest spatter count, such that the maximum value across the build plate is 1. The concentration is normalized to compare with the spatter model, which does not release the same number of particles as the experiment due to modeling limitations. Spatter particles that land within part boundaries are not visible from experimental data because the algorithm masks parts from the image before detecting spatter particles on the powder bed, as mentioned in Section 3.2.

When looking at all spatter particles detected in the experiment in Fig. 7(a), it seems that spatter particles do not travel far from their ejection point. There is a high concentration of spatter particles immediately downstream from the parts. Most spatter particles land within about 50 mm downstream from the parts, with fewer landing to the left and right of the part.

Parts closer to the outlet show a slightly higher spatter concentration around them, which could suggest that either spatter particles travel shorter distances in that region, or that spatter particles land more often in that region. The velocity near the outlet in Fig. 6 is not very different from the rest of the build area, so spatter particles will not have shorter travel distances if they are ejected near the outlet. Instead, results from Zhang et al. [36] suggest that a step height at the outlet will make it more difficult for the flow to transport some spatter particles out from the machine. There is a step height in the EOS M290 (seen best in Fig. 6(a)), so the increased bunching of particles near the outlet is most likely a result of the outlet's height.

The spatter model ejected 3.6 million particles, which is less than what the IR camera detected. This will not affect the accuracy of this comparison because the spatter concentrations are normalized for the experiment and the model. Normalization scales the results to lie between 0 and 1, preserving areas with high concentration and allowing for a quantitative comparison. When calculating the spatter concentration with the results from the spatter model, weights based on particle diameter are applied. This is done to make the model's ejected size distribution mimic those shown in literature. This work specifically follows the size distributions shown in Gasper et al. [22]. The method through which these weighting factors are calculated is discussed in detail in Appendix.

Fig. 7(b) shows how the concentration of spatter from the spatter model has some trends similar to the experiment's. For example, the highest concentration of spatter occurs immediately downstream from

the parts, and there is a relatively lower concentration between the parts. The model also shows a bunching of spatter near the outlet.

Despite similar trends between the model and the experiment, the model overall suggests more spatter contamination than what is shown in the experiment. In addition to this difference, a stripe of high spatter concentration appears on the right side of the build area, which is a distinctive feature not seen in the experimental data.

To demonstrate the cause of these features, the spatter concentration from the model was altered such that only spatter particles above 310 K were included in the spatter concentration. Removing those particles mimics how the IR camera cannot detect particles that are too close to the powder bed temperature.⁸ For reference, all spatter particles are released at Inconel 718's melt temperature of 1,673 K [50], and the gas temperature is 300 K throughout.

After removing particles colder than 310 K, the spatter concentration shown in Fig. 7(c) looks more similar to the experiment in Fig. 7(a). The lower concentration of spatter between parts is captured more accurately in the model, and no unexpected features exist. While the concentration in the model is still higher than the experiment overall, most spatter particles seem to travel about 75 mm in the downstream direction: similar to that seen in the experiment.

Spatter particles from the experiment are detected by the IR camera because they are hotter (more emissive) compared to the powder bed surrounding them. Therefore, the IR camera will be less likely to detect particles that are too close to the powder bed's temperature, and these particles will not be included in the experiment's spatter concentration. The spatter that landed in the stripe of high concentration from Fig. 7(b) was comprised of these colder particles and would have been too cold to be seen by the IR camera. This is a probable reason that the experiment in Fig. 7(a) showed less spatter concentration than the simulation's heatmap in Fig. 7(b).

These colder particles landed in the stripe pattern in the simulation because they probably had a longer flight time, a smaller diameter, and/or a faster ejection speed than the particles that were hotter than 310 K.⁹ Spatter particles with a higher velocity in the y -direction would reach a higher height in the machine, making them more likely to be affected by the clashing flow fronts identified in Fig. 6(b). As will be discussed in Section 4.4, spatter particles with a smaller diameter will follow the flow more closely than larger particles. Combining these two ideas, the small, fast particles could thus be pushed towards the stripe pattern, but large, fast particles would not. Smaller particles would also cool faster than larger particles because of their difference in thermal mass, which explains why the stripe pattern disappeared in Fig. 7(c), where the coldest spatter particles were removed.

There is still some uncertainty in the spatter that is detected by the IR camera, but the current extent of the comparison is sufficient to demonstrate the performance of the spatter model as a tool that could predict spatter contamination for a build cycle. Furthermore, due to the accuracy of the flow model and the spatter model's accuracy control metrics, the spatter model is still likely accurate when predicting the trajectory of a particle with a specific diameter, density, and velocity, as will be done in Section 4.4.

4.4. Spatter transport according to diameter, velocity, and density

The forces vital to spatter transport are proportional to a spatter particle's diameter, velocity, and material density, as shown in Eq. (12) (Section 2.3). This section investigates how these model parameters affect the transport of spatter, with the intention that this will show

⁸ 310 K is chosen as an example and does not imply that 310 K is the cutoff temperature at which the experiment's IR algorithm cannot detect a spatter particle.

⁹ This is deduced from looking at the terms that affect the temperature calculation in Eq. (14).

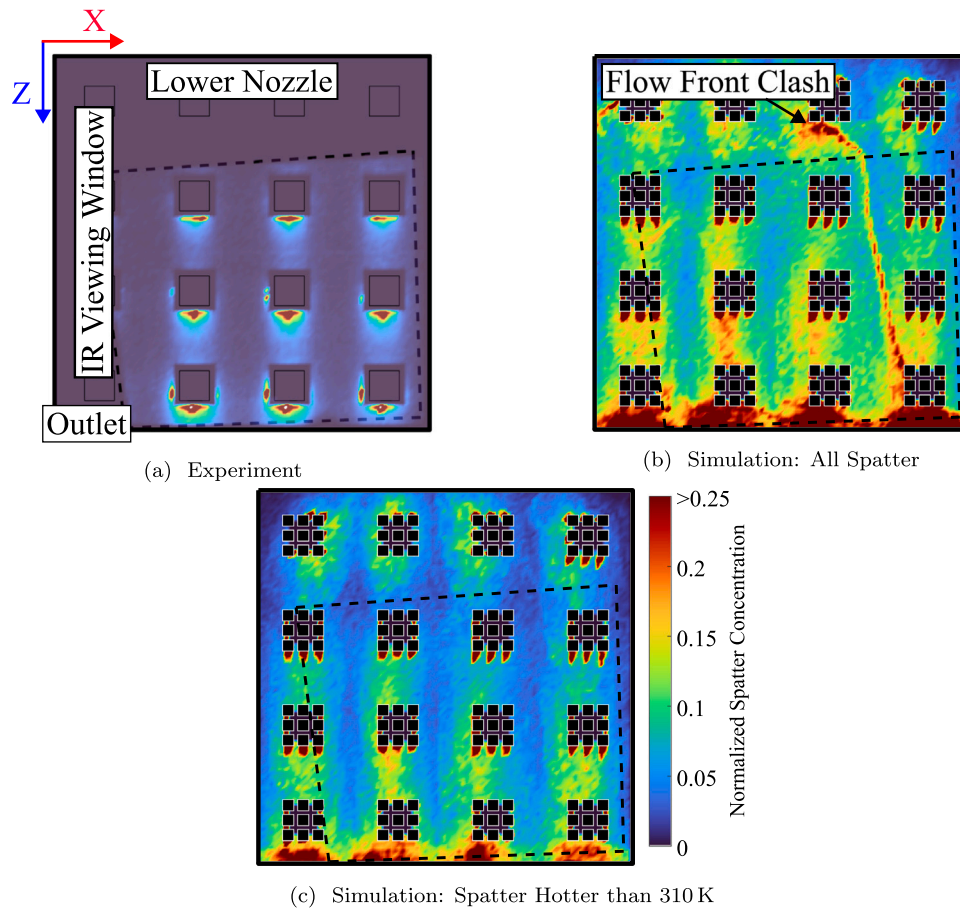


Fig. 7. Spatter concentration from spatter experiment and spatter model. Each graph shares the same colorscale, shown in Fig. 7(c). The black dashed line indicates the area that was visible with the IR camera, as indicated in Fig. 7(a). For reference, the gas temperature was assumed to be constant at 300K in the simulation. The black borders indicate the extent of the build area in each subfigure. These figures should all be viewed in color for best results.

which spatter particles are best removed by the gas flow. Spatter particles are ejected from the 25×25 source grid (see Fig. 3 in Section 2.3) in a flow of argon with a setting of 81 Pa (6.5 m/s).

Particles with larger diameters are theorized to be an immediate cause behind LOF defects in AM (as discussed in Section 1). The spatter model predicts that fewer of the larger defect-causing spatter particles are removed by the flow, as illustrated in Fig. 8(a). Nearly 75% of 200 μm particles landed in the build area, compared to only 50% of 25 μm particles. These larger particles also travel less than the smaller particles. Nearly all 200 μm spatter particles land within 110 mm of the source, while most of the 25 μm spatter particles land farther away, within 175 mm of the source.

According to this work, larger particles travel less distance and are less likely to exit the machine than smaller particles, which is an issue considering that the larger particles are the ones that are linked to immediate defects in parts. This relationship occurs because of the tradeoff between drag and gravity forces as a function of particle diameter. Gravity force is cubically proportional to a particle's diameter, while drag force is only quadratically proportional. Gravity force will be more significant than drag force for larger particles. This tradeoff can be represented by the Stokes number, Stk :

$$Stk = \frac{\tau_p}{\tau_f} \quad \text{where} \quad \tau_p = \frac{\rho_p D_p^2}{18\mu} \quad \text{and} \quad \tau_f = \frac{\Delta z}{|u_f|} \quad (17)$$

where τ_p is the response time of the particle's velocity, and τ_f is a characteristic response time of the fluid's velocity [70]. Crowe et al. [70] interprets the Stokes number as a measure of how well a particle will follow the velocity of the fluid surrounding it. When $Stk \ll 1$, the

response time of the particle is much smaller than the fluid, and the particle is more likely to follow the streamlines of the flow and have a velocity equal to the flow surrounding it. On the other side, $Stk \gg 1$ indicates that the difference in the particle and the flows response times is too great for the particle to follow the flow precisely, so the particle will deviate from the flow vectors and will not have a velocity equal to the fluid surrounding it. The current work uses the Stokes number for comparative purposes to show which type of particle will follow the streamlines of the flow more closely.

Fig. 6(a) shows that the flow generally points towards the outlet, so a particle with a Stokes number larger than 1 would not follow the flow vectors and would not be pushed as far as a particle with a smaller Stokes number (so long as ejection speed and angle are identical). A 25 μm and a 200 μm particle have approximate Stokes numbers of 0.1 and 6.8, respectively,¹⁰ which explains why the two particle sizes differ so greatly in their travel distance and removal rate.

This trend is demonstrated in Fig. 8(b), which plots the landing locations of spatter particles ejected from the center of the build area. It is apparent that the smaller particles travel further in the downstream direction and travel less in the transverse direction. Conversely, the larger particles do not follow the flow's streamlines as closely, so they land in a more circular shape. In other words, the effect of drag force on

¹⁰ The response time of the fluid is not well-defined by Crowe et al. [70], so this work approximates it by the time it would take for fluid to traverse the build area; the characteristic flow speed is assumed to be $|u_f| = 2\text{ m/s}$ (see Fig. 6(a)), and the build area is $\Delta z = 250\text{ mm}$ long.

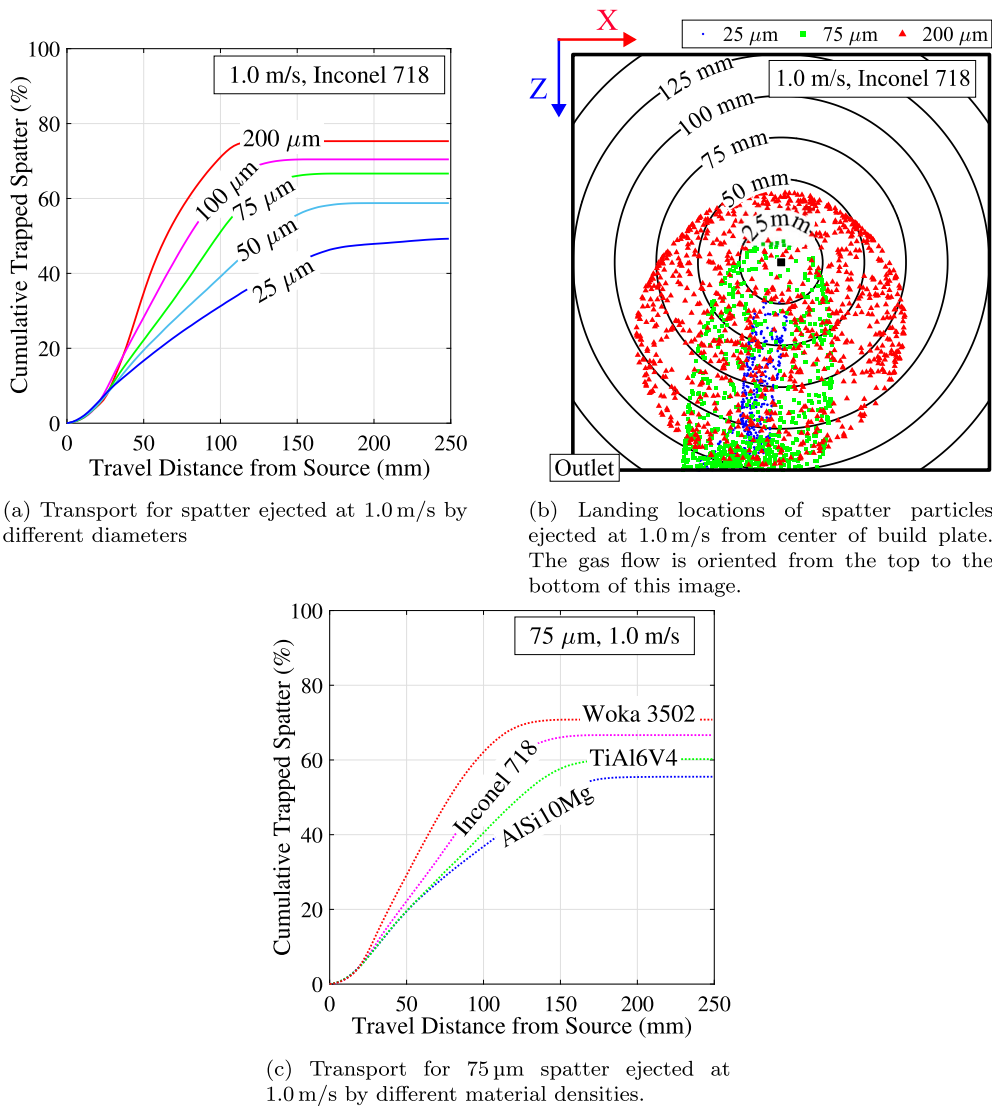


Fig. 8. Travel distance from ejection source by different characteristics of spatter particles. Please note that these plots are cumulative, meaning they represent the amount of spatter particles that reached that distance or less.

larger particles is less than the effect of drag force on smaller particles because larger particles are less responsive.

The Stokes number also explains how changing particle density will affect its travel distance. A 75 μm particle with the density of AlSi10Mg versus the density of Woka 3502 will have Stokes numbers of 0.3 and 1.6, respectively. Spatter particles with a density of Woka 3502 will be less affected by the drag force than particles with that of AlSi10Mg, albeit the difference is smaller than that shown for a difference in diameter. This trend is demonstrated by the model's results in Fig. 8(c). Comparing the particles with densities of AlSi10Mg and Woka 3502, the total amount of spatter landing on the build area only goes from about 55% to 70%, respectively. In other words, an increase in density by about six times (from AlSi10Mg to Woka 3502) only results in 15% more spatter left behind by the flow. Compare this with trends from Fig. 8(a), where an increase in diameter from 25 μm to 200 μm (an increase of eight times), results in 25% more spatter being left behind in the machine. The distance traveled by a spatter particle similarly only decreases marginally with density: the densest spatter lands within 125 mm of its source, versus 160 mm for the lightest. Essentially, changing a particle's density would affect the trajectory of the particle, but it would not affect it as significantly as the particle's diameter.

The trajectory of a particle is also affected by its initial velocity. Fig. 9 shows how a particle's speed and elevation angle affect travel distance. This plot shows the landing locations of particles from just a single source. Travel distance is obtained by the rings surrounding the central source. Particles ejected at 0.5 m/s (these are the particles forming the tightly-packed elliptical shape in Fig. 9(b)) all land within about 90 mm of their source. Out of the particles ejected at 0.5 m/s, Fig. 9(a) shows that the particles that travel the farthest are those with a high elevation angle, likely because this gives them the most time in the lower nozzle's flow.¹¹

Particles ejected at 1 m/s (these are the particles that form the larger elliptical shape in Fig. 9(b)) travel further than the 0.5 m/s particles, but they begin to bunch up at the foot of the outlet. Particles with a higher speed will travel further than those with a lower speed due to having higher initial momentum, but this will only be true up to a certain point. After a certain ejection speed, spatter particles will break through the lower nozzle's jet and be affected by the large vortex in Fig. 6. This

¹¹ This is a fact that can be demonstrated with the equations of projectile motion; a particle ejected straight upwards will have the longest flight time compared with any other ejection angle.

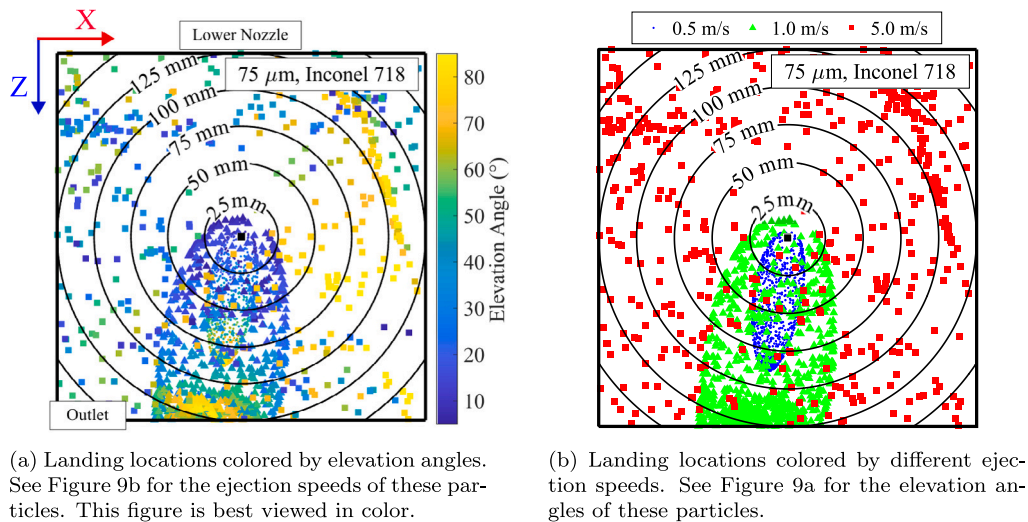


Fig. 9. Landing locations of $75\ \mu\text{m}$ spatter particles ejected for different speeds and elevation angles. Spatter is only ejected from the black source in the center of the plot. The rings in the plot identify the distance from that central source. The black borders indicate the extent of the build area in both subfigures.

is illustrated in the particles ejected at $5\ \text{m/s}$, which scatter over the build area in a chaotic pattern instead of landing in an elliptical shape. This would mean that particles ejected with a speed between $1\ \text{m/s}$ and $5\ \text{m/s}$ will break out of the lower nozzle jet, and they will travel in a less predictable pattern. Spatter particles ejected at these higher speeds are likely too small to be captured by a sieve, and as discussed in Section 1, they could cause LOF or reduced material properties if they end up in the reused powder.

Initial research has shown that a spatter particle's diameter, initial speed, and elevation angle may be affected by laser parameters. For example, results from Bidare et al. [25] demonstrate that a higher laser power will create a stronger plume, which might cause larger particles to be ejected from the melt-pool as entrainment spatter. The direction of the vapor plume is shown to change with laser power and speed by results in Ly et al. [13], which could mean that the elevation angle of particles would also change with laser settings. Finally, results from Yin et al. [23] and Gunenthiram et al. [24] both show some results regarding the general change in the diameter, initial speed, and ejection angle of spatter particles as a function of laser settings as well.

The research on the relationship between laser settings and spatter production does not seem to be conclusive, but the results from this current work would suggest that controlling laser parameters could be another effective strategy in reducing spatter contamination. Producing smaller particles will allow them to follow the streamlines of the flow more closely and to travel towards the outlet. This may result in more spatter removal and fewer immediate LOF defects caused by large spatter particles. The ejection velocity of a spatter particle will also affect how well the particle is transported by the flow, so choosing a laser speed that produces fewer slow particles would be advantageous. Because the difference between the spatter left behind for the lightest and heaviest AM alloys was not significant, it is predicted that these suggested approaches would apply to each of the AM alloys discussed in this work.

4.5. Effects of ejection location and gas flow rate on spatter transport

The results in this section were obtained for Inconel 718 spatter, which is ejected from the 25×25 grid of sources (see Fig. 3 in Section 2.3) in a flow of argon gas with a setting of $81\ \text{Pa}$ ($6.5\ \text{m/s}$).

Spatter ejected near the lower nozzle is less likely to be transported out of the machine. This is demonstrated by the result in Fig. 10(a), which displays the percent of spatter that landed back on the build plate for each ejection source. Nearly 40% of spatter particles ejected

near the outlet land back on the build area versus 80% of the spatter particles ejected from near the nozzle. This occurs in tandem with the results from Section 4.4, which show that most spatter particles in the model travel only up $150\ \text{mm}$ from its ejection source.

A factor that may also contribute to the low removal rate of spatter near the lower nozzle is related to the flow itself. As discussed in Section 4.2, there is a low-speed zone directly beneath the lower nozzle; spatter particles that are ejected within this zone will experience a low drag force and will thus not be transported as far as other spatter particles. The effect of the low-speed zone on spatter transport is demonstrated in Fig. 10(b), which plots the landing locations of spatter particles ejected from three locations: one in the top-left, one in the top-center, and one in the center of the build area. The dense region of spatter particles near the central source exhibits a shape similar to Fig. 9 from Section 4.4. The elongated shape is attributable to the flow speed in that area, which transports spatter towards the outlet. Most of the spatter ejected from the top row of sources lands in a circular pattern with no significant downstream movement. Compared with the central source's spatter, these results suggest that the low-speed zone impedes spatter transport.

Alternatively, the transverse movement of spatter (to the left and right) is not affected by the low speed zone. Fig. 10(b) shows that the width of the contaminated area near the central source is identical to the other sources shown in the top row. This suggests that most of the spatter particles in the spatter model do not travel transverse to the flow more than $50\ \text{mm}$, even if they travel closer to $150\ \text{mm}$ in the downstream direction.

Intelligent part placement could be a strategy to avoid spatter contamination. Spatter particles are more likely to contaminate parts that are downstream from their ejection source rather than to the source's left or right, so avoiding placing parts upstream or downstream from one another could reduce inter-part spatter contamination. This suggested strategy can also be gathered from our own experiment, where the regions of lowest contamination were seen between parts and the highest contamination were downstream from parts (see Fig. 7(a)). Similarly, Snow et al. [34] conducted an experiment that showed a significant amount of spatter contamination for parts downstream from a "Spatter Generator", but parts to the right of this "Spatter Generator" did not become contaminated significantly. Similar conclusions can be drawn from the results in Schwerz et al. [35].

The spatter model seems to concur with the trends in this work's own experiment and other experiments in literature. Therefore, based on the spatter model's results, a good strategy to reduce spatter contamination may also be to arrange parts in a staggered fashion, with at

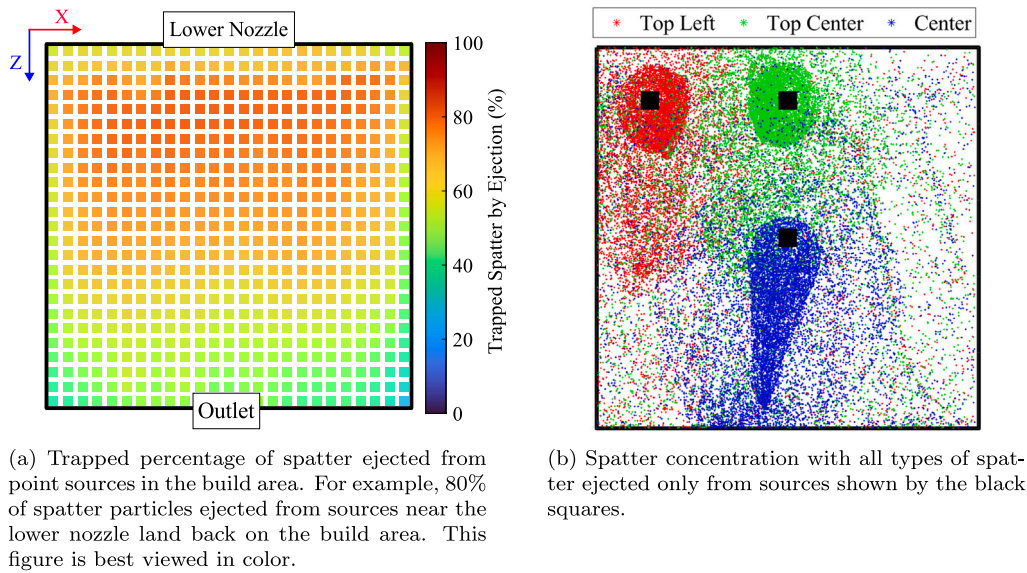


Fig. 10. Spatter particle landing locations on the build area. Black squares indicate the sources from which spatter particles in this figure were ejected. The black borders indicate the extent of the build area in both subfigures.

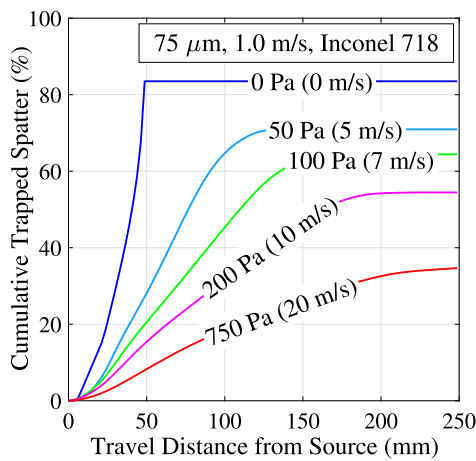


Fig. 11. Travel distance from ejection source for different machine pressure differentials. Please note that this plot is cumulative, meaning the values represent the amount of spatter particles that reached that distance or less.

least 25 mm between them in the transverse direction, while avoiding placing any parts downstream from one another.¹² Please note that this approach will not eliminate the issue discussed in Section 1 regarding reusing powder. Small spatter may still land on the powder, contaminating it if the powder is reused for later build cycles.

With the current nozzle design, the low-speed zone will always exist. Parts underneath the nozzle will most likely always suffer from less spatter removal, but changing the machine’s pressure differential setting (i.e., changing the gas flow rate) can improve spatter transport for parts located outside of this region. The following results track the amount of spatter left behind in the build area for the following pressure differentials: 0 Pa, 50 Pa, 100 Pa, 200 Pa, and 750 Pa. These settings correspond to inlet velocities of 0 m/s, 5.1 m/s, 7.3 m/s, 10.3 m/s, and 20.0 m/s, respectively. The former three settings are within the range of

¹² The inverse of this strategy would be to change the direction of the gas flow such that no parts are being printed downstream from one another.

the EOS M290 (the nominal for Inconel 718 is 81 Pa (6.5 m/s)), and the latter two are outside of it. Only Inconel 718 spatter particles of 75 μm diameter and 1.0 m/s ejection speed are ejected in this comparison. All other conditions are kept the same.

Increasing differential pressure removes more spatter and carries it further, as shown in Fig. 11. At 0 Pa, without any assistance from the lower nozzle jet, 82% of the ejected spatter particles remain in the build area. Increasing to half of the maximum flow setting at 50 Pa reduces this to 70%. The increase in travel distance is also significant. The furthest a particle travels in 0 Pa is 50 mm; this increases to 125 mm at 50 Pa.

Despite these large gains from no flow to half of the maximum setting, increasing to the maximum flow setting of 100 Pa only yields a marginal increase over 50 Pa. Only 65% of spatter particles are removed at the maximum setting, and they only travel an additional 25 mm away from their ejection source. Most AM machine users will likely use a flow setting between 50 Pa and 100 Pa, so this suggests that there are diminishing returns with increasing the differential pressure.

Future iterations may benefit from an increased flow speed, though. Increasing the differential pressure to 750 Pa would only allow about 37% of spatter particles to land in the build area, with some of them traveling the entire length of the build plate. This increased flow speed would certainly assist in removing spatter particles from parts that are printed near the lower nozzle.

While this increase to differential pressure is an intuitive strategy, it will likely cause more issues by disturbing the powder bed. Shen et al. [71] has shown how powder pickup varies with several AM powder sizes and materials. Shen used a 30 mm vane anemometer to measure the flow speed above the powder bed in a different L-PBF machine. They correlated this flow speed to powder pickup and found that nickel-based powders, like Inconel 718, were picked up between 5.2 m/s and 5.7 m/s. These vane anemometer measurements are approximated in the model by calculating an average velocity at location A (this is visible in Fig. 5 in Section 4.1). The average includes only points from 0 to 30 mm above the build area to mimic the 30 mm vane anemometer.

The resulting average speeds at this location for 100 Pa, 200 Pa, and 750 Pa are 1.9 m/s, 2.5 m/s, and 5.4 m/s, respectively. At 750 Pa, the predicted flow speed enters the range of bulk powder pickup identified in Shen et al. [71], showing that this machine setting may be just

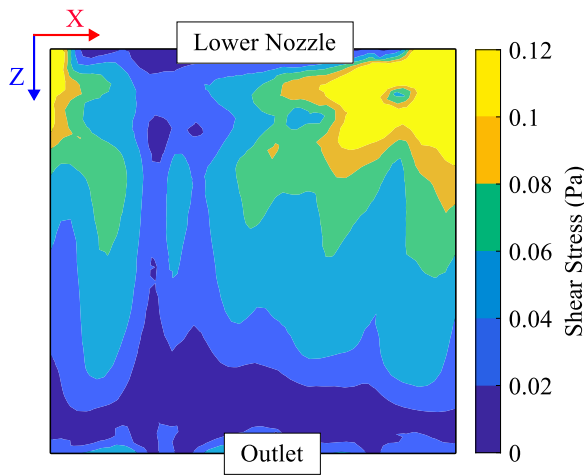


Fig. 12. Shear stress over build area for 100Pa machine setting (velocity inlet of 7.3 m/s). The black borders indicate the extent of the build area.

over the safe powder pickup limit. However, this does not mean that a machine setting of 200 Pa would be safe to use.

Powder pickup is initiated by the shear stress between the gas and the powder bed [72], so local maxima of the fluid shear stress on the powder bed may initiate powder denudation even when bulk powder pickup is not expected. Many empirical relations use flow-speed measurements (like in Shen et al. [71]) because shear stress is difficult to measure directly in experiments, but Shao and Lu [73] have developed an expression for the threshold friction velocity, u_t^* , on a mono-dispersed (single diameter) powder bed. The following equation converts their expression into one for the critical powder pickup shear stress, $\tau_{w,t}$:

$$\tau_{w,t} = u_t^{*2} \rho_p = A_N \left(\rho_p |g| D_p + \frac{\gamma}{D_p} \right) \quad (18)$$

A_N and γ are empirical constants, which are 1.23×10^{-2} and $3 \times 10^{-4} \text{ kg/s}^2$, respectively [73]. This model incorporates the effects of cohesive forces between the particles and the effect of a particle's mass. The major assumption of this model is the mono-dispersed nature of the powder bed; most powders in AM are poly-dispersed, having a continuous distribution of particle diameters. Anantharaman et al. [74] showed that bi-dispersed powders are picked up at flow speeds closer to the larger of the two particle sizes. Extrapolating from Anantharaman's results, Shao and Lu's model can thus still be used, keeping in mind that a powder of mixed diameters will have a critical shear stress closer to the largest of the powder's diameters.

According to Eq. (18), a powder bed of $75 \mu\text{m}$ Inconel 718 particles will be disturbed once the shear stress reaches 0.123 Pa. Using the conclusion from Anantharaman et al. [74], this analysis assumes that the powder bed will be disturbed at approximately this shear stress.

The shear stress on the build plate for the 100 Pa flow setting is shown in Fig. 12. The shear stress has a non-uniform distribution over the build area. The limit of the colormap is chosen to be near the critical powder pickup shear stress according to Shao and Lu's model [73]. The patterns that occur in this colormap are related to the flow contours 5 mm above the build area in Fig. 6(b). Regions with a rapidly changing flow speed would experience higher shear stress, which is why the shear stress is higher where the velocity near the build plate is higher in Fig. 6(b).

The high shear in the upper right and left corners occur because of the higher speeds in those areas. The local high shear stresses will likely move powder and disrupt the powder bed at higher pressure differential settings, resulting in powder bed defects. While higher flow

rates may remove more spatter, they will also remove the powder that is required to print. Approaches to increase the powder pickup limit could be useful, for they would enable higher flow rates and lead to the removal of more spatter particles from the machine.

5. Summary and conclusions

In this work, a computational fluid dynamics (CFD) model was coupled with the discrete phase model (DPM) in ANSYS Fluent 2021 R2 to predict the gas flow and spatter transport within an EOS M290 L-PBF machine. This machine is used as an example because it is similar to many other L-PBF machines. Experimental measurements were used to validate the model's flow and spatter predictions. This model was subsequently used to investigate (1) the development of the flow in the machine, (2) the transport of spatter particles with varying diameters, speeds, ejection angles, and material densities, (3) the effects of part placement on spatter transport, and (4) the effects of gas flow rate on spatter transport.

The machine's design features tended to produce a nonuniform flow over the build area. This is attributed to the height of the lower nozzle and the height of the outlet, both of which caused low-speed zones in the adjacent regions. The low-speed zone near the lower nozzle covered the top 50 mm of the build area. This low-speed zone was shown to not transport spatter as effectively as the rest of the flow over the build area, leaving most spatter landing within 50 mm of where it was ejected. The authors' recommendation is to consider this region of the build area as unique from the rest of the build area due to the difference in flow conditions at this region. Parts printed in this region may have different properties compared to parts from other regions of the build area. Changing the design of the nozzle could remove this low-speed region, although this option may not be accessible to all AM machine users in a timely fashion.

Spatter diameter and velocity were found to be major factors in determining a particle's travel distance. Larger particles are less likely to follow the flow and will travel shorter distances than smaller particles, all other factors being equal. For velocity, faster particles will travel farther than slower ones. The material density of spatter particles did not have as drastic an influence on spatter transport as diameter or velocity, suggesting that even the lightest of AM materials is subject to spatter contamination. Where spatter particle diameter and velocity can be controlled via laser parameters, it is likely best to produce small, fast particles, for those are predicted to travel the farthest and be most likely to be removed from the build area, regardless of material.

In general, most spatter particles landed within 150 mm downstream from their ejection location at the nominal flow setting for Inconel 718 with argon of 81 Pa (6.5 m/s). Transverse to the flow, particles traveled only about 50 mm. These results demonstrate that parts can be placed during build planning such that they do not contaminate one another with spatter. For instance, placing parts next to one another rather than downstream from one another will likely prevent a majority of spatter contamination in the parts from that build cycle.

It is worth mentioning a couple caveats to this approach, however. This approach will limit the build rate of the machine compared with an approach that fits as many parts in the machine as possible. Furthermore, larger parts (those with a wider coverage of the build area) would not benefit as much from this strategy and may self-contaminate throughout the build cycle. Finally, this approach does not eliminate the issue of the unused powder being possibly contaminated by smaller spatter particles. These are all issues that require further investigation.

Finally, increasing flow rate as an approach to removing spatter was found to be promising, but only if powder pickup is not a limitation. A flow rate of 750 Pa (20 m/s), which currently is not allowed, would remove 30 % more spatter than the current max setting of 100 Pa (7.3 m/s). These gains are substantial, but it was also predicted that local regions of the powder bed would be disturbed by the flow, even at the max setting. Increasing beyond the current max setting is limited by powder pickup. Increasing the forces that keep powder on the powder bed would allow for increases to the machine's flow rate without disrupting the powder bed.

CRedit authorship contribution statement

Nicholas O'Brien: Software, Writing – original, Review & editing, Investigation. **Syed Zia Uddin:** Investigation, Validation. **Jordan Weaver:** Investigation, Validation. **Jake Jones:** Resources. **Satbir Singh:** Methodology, Supervision. **Jack Beuth:** Funding, Project administration, Review, Conceptualization.

Declaration of competing interest

The authors declare the following financial interests/personal relationships which may be considered as potential competing interests: Jack Beuth, Nicholas O'Brien, Syed Zia Uddin reports financial support was provided by US Department of Defense. If there are other authors, they declare that they have no known competing financial interests or personal relationships that could have appeared to influence the work reported in this paper.

Data availability

Data will be made available on request.

Acknowledgments

A portion of this research was sponsored by the Army Research Laboratory and was accomplished under Cooperative Agreement Number W911NF-20-2-0175. The views and conclusions contained in this document are those of the authors and should not be interpreted as representing the official policies, either expressed or implied, of the Army Research Laboratory or the U.S. Government. The U.S. Government is authorized to reproduce and distribute reprints for Government purposes notwithstanding any copyright notation herein.

This work used the Extreme Science and Engineering Discovery Environment (XSEDE) [75], which is supported by National Science Foundation, United States grant number ACI-1548562. Specifically, it used the Bridges-2 system [76], which is supported by NSF award number ACI-1928147, at the Pittsburgh Supercomputing Center (PSC). This project was completed under the charge ID MCH220004P. The authors thank David O'Neal and T.J. Olesky for their assistance with configuring ANSYS Fluent 2021 on the Bridges-2 system. The authors would also like to acknowledge Dr. Christian Gobert and Dr. Brandon Abranovic for sharing each of their expertise while working on this project.

Appendix. Discussion of weighting factors for following spatter size distributions

This is a continuation of the discussion started in Section 4.3. The diameters of spatter particles ejected by the spatter model do not initially follow those shown in literature (Gasper et al. is an example [22]). This is remedied through weighting factors, which are applied to each particle while calculating the spatter concentration.

First, the distribution for each diameter must be normalized because the model ejects more particles of some diameters than others. For example in Table 2 (in Section 2.3), 6000 75 μm particles are ejected versus 3000 100 μm particles. Without normalizing the distributions, the spatter concentration would be biased towards 75 μm , which would possibly under-represent the amount of other particle sizes. Normalization is accomplished by assigning each particle in the spatter model a weight that is set equal to the reciprocal of the number of particles ejected per diameter, per source (e.g., 1/6000 for 75 μm).

Once the first normalizing factor is applied, each particle must then be weighted with an additional factor to account for the fact that some diameters will statistically occur more often than others during the L-PBF process. According to results from Gasper et al. [22], 75 μm spatter accounts for 5.1% to 7.4% of all spatter particles recovered across

Table A.4

Weights for spatter model's spatter concentration.

Diameter (μm)	Weight 1	Weight 2	Final Weight ($\times 10^3$)
25	1/5000	3.65	0.73
50	1/5000	10.85	2.17
75	1/6000	6.25	1.04
100	1/3000	3.35	1.12
150	1/3000	1.05	0.35
200	1/3000	0.40	0.13

several machines, so the additional weighting factor that would be applied to all 75 μm particles would be the average of Gasper's results: 6.25. The weighting factors for other diameters of spatter are similarly informed by results from Gasper et al. [22].

The two weighting factors are multiplied together to achieve a final weighting factor for each particle. Table A.4 summarizes each of the weighting factors by diameter. When a spatter particle is counted in the spatter concentration metric, it adds the weighting factor to that bin's value instead of 1. This weighting is done before the spatter concentration is normalized by the maximum concentration, so only the relative magnitudes of the weights will affect the final spatter concentration. Please note that this weighting approach is performed only for the results presented in Section 4.3 to better mimic the conditions of the experiment. The authors acknowledge that spatter velocities likely have a distribution, but it is not known and is assumed to take on the distribution as it is shown in Table 2 (in Section 2.3).

References

- [1] C. Sun, Y. Wang, M.D. McMurtrey, N.D. Jerred, F. Liou, J. Li, Additive manufacturing for energy: A review, *Appl. Energy* 282 (2021) 116041, <http://dx.doi.org/10.1016/j.apenergy.2020.116041>, URL <https://linkinghub.elsevier.com/retrieve/pii/S030626192031477X>.
- [2] S. Chowdhury, N. Yadaiah, C. Prakash, S. Ramakrishna, S. Dixit, L.R. Gupta, D. Buddhi, Laser powder bed fusion: A state-of-the-art review of the technology, materials, properties & defects, and numerical modelling, *J. Mater. Res. Technol.* (2022) S2238785422011607, <http://dx.doi.org/10.1016/j.jmrt.2022.07.121>, URL <https://linkinghub.elsevier.com/retrieve/pii/S2238785422011607>.
- [3] Z. Li, H. Li, J. Yin, Y. Li, Z. Nie, X. Li, D. You, K. Guan, W. Duan, L. Cao, D. Wang, L. Ke, Y. Liu, P. Zhao, L. Wang, K. Zhu, Z. Zhang, L. Gao, L. Hao, A review of spatter in laser powder bed fusion additive manufacturing: In situ detection, generation, effects, and countermeasures, *Micromachines* 13 (8) (2022) 1366, <http://dx.doi.org/10.3390/mi13081366>, URL <https://www.mdpi.com/2072-666X/13/8/1366>.
- [4] U. Ali, R. Esmailizadeh, F. Ahmed, D. Sarker, W. Muhammad, A. Keshavarzkermani, Y. Mahmoodkhani, E. Marzbanrad, E. Toyserkani, Identification and characterization of spatter particles and their effect on surface roughness, density and mechanical response of 17-4 PH stainless steel laser powder-bed fusion parts, *Mater. Sci. Eng. A* 756 (2019) 98–107, <http://dx.doi.org/10.1016/j.msea.2019.04.026>, URL <https://linkinghub.elsevier.com/retrieve/pii/S0921509319304721>.
- [5] Y. Liu, Y. Yang, S. Mai, D. Wang, C. Song, Investigation into spatter behavior during selective laser melting of AISI 316L stainless steel powder, *Mater. Des.* 87 (2015) 797–806, <http://dx.doi.org/10.1016/j.matdes.2015.08.086>, URL <https://linkinghub.elsevier.com/retrieve/pii/S0264127515303361>.
- [6] D. Greitemeier, C. Dalle Donne, F. Syassen, J. Eufinger, T. Melz, Effect of surface roughness on fatigue performance of additive manufactured Ti-6Al-4V, *Mater. Sci. Technol.* 32 (7) (2016) 629–634, <http://dx.doi.org/10.1179/1743284715Y.0000000053>, URL <https://www.tandfonline.com/doi/full/10.1179/1743284715Y.0000000053>.
- [7] R. Esmailizadeh, U. Ali, A. Keshavarzkermani, Y. Mahmoodkhani, E. Marzbanrad, E. Toyserkani, On the effect of spatter particles distribution on the quality of Hastelloy X parts made by laser powder-bed fusion additive manufacturing, *J. Manuf. Process.* 37 (2019) 11–20, <http://dx.doi.org/10.1016/j.jmpro.2018.11.012>, URL <https://linkinghub.elsevier.com/retrieve/pii/S1526612518303979>.
- [8] C. Kantzos, J. Pauza, R. Cunningham, S.P. Narra, J. Beuth, A. Rollett, An investigation of process parameter modifications on additively manufactured Inconel 718 parts, *J. Mater. Eng. Perform.* 28 (2) (2019) 620–626, <http://dx.doi.org/10.1007/s11665-018-3612-3>, URL <http://link.springer.com/10.1007/s11665-018-3612-3>.
- [9] A. Mostafaei, C. Zhao, Y. He, S. Reza Ghiaasiaan, B. Shi, S. Shao, N. Shamsaei, Z. Wu, N. Kouraytem, T. Sun, J. Pauza, J.V. Gordon, B. Webler, N.D. Parab, M. Asherloo, Q. Guo, L. Chen, A.D. Rollett, Defects and anomalies in powder bed fusion metal additive manufacturing, *Curr. Opin. Solid State Mater. Sci.* 26 (2) (2022) 100974, <http://dx.doi.org/10.1016/j.cossms.2021.100974>, URL <https://linkinghub.elsevier.com/retrieve/pii/S1359028621000772>.

- [10] T. Ohtsuki, L. Smith, M. Tang, P.C. Pistorius, Origin of oxides and oxide-related pores in laser powder bed fusion parts, in: N. Shamsaei, M. Seifi (Eds.), *Structural Integrity of Additive Manufactured Materials & Parts*, ASTM International, 100 Barr Harbor Drive, PO Box C700, West Conshohocken, PA 19428-2959, 2020, pp. 45–60, <http://dx.doi.org/10.1520/STP163120190137>, URL <https://www.astm.org/doiLink.cgi?STP163120190137>.
- [11] J.V. Gordon, S.P. Narra, R.W. Cunningham, H. Liu, H. Chen, R.M. Suter, J.L. Beuth, A.D. Rollett, Defect structure process maps for laser powder bed fusion additive manufacturing, *Addit. Manuf.* 36 (2020) 101552, <http://dx.doi.org/10.1016/j.addma.2020.101552>, URL <https://linkinghub.elsevier.com/retrieve/pii/S2214860420309246>.
- [12] R. Cunningham, S.P. Narra, C. Montgomery, J. Beuth, A.D. Rollett, Synchrotron-based X-ray microtomography characterization of the effect of processing variables on porosity formation in laser powder-bed additive manufacturing of Ti-6Al-4V, *JOM* 69 (3) (2017) 479–484, <http://dx.doi.org/10.1007/s11837-016-2234-1>, URL <http://link.springer.com/10.1007/s11837-016-2234-1>.
- [13] S. Ly, A.M. Rubenchik, S.A. Khairallah, G. Guss, M.J. Matthews, Metal vapor micro-jet controls material redistribution in laser powder bed fusion additive manufacturing, *Sci. Rep.* 7 (1) (2017) 4085, <http://dx.doi.org/10.1038/s41598-017-04237-z>, URL <http://www.nature.com/articles/s41598-017-04237-z>.
- [14] X. Li, C. Zhao, T. Sun, W. Tan, Revealing transient powder-gas interaction in laser powder bed fusion process through multi-physics modeling and high-speed synchrotron X-ray imaging, *Addit. Manuf.* 35 (2020) 101362, <http://dx.doi.org/10.1016/j.addma.2020.101362>, URL <https://linkinghub.elsevier.com/retrieve/pii/S221486042030734X>.
- [15] M. Tang, P.C. Pistorius, J.L. Beuth, Prediction of lack-of-fusion porosity for powder bed fusion, *Addit. Manuf.* 14 (2017) 39–48, <http://dx.doi.org/10.1016/j.addma.2016.12.001>, URL <https://linkinghub.elsevier.com/retrieve/pii/S2214860416300471>.
- [16] M. Laleh, A.E. Hughes, S. Yang, J. Wang, J. Li, A.M. Glenn, W. Xu, M.Y. Tan, A critical insight into lack-of-fusion pore structures in additively manufactured stainless steel, *Addit. Manuf.* 38 (2021) 101762, <http://dx.doi.org/10.1016/j.addma.2020.101762>, URL <https://linkinghub.elsevier.com/retrieve/pii/S2214860420311349>.
- [17] C. Zhao, Q. Guo, X. Li, N. Parab, K. Fezzaa, W. Tan, L. Chen, T. Sun, Bulk-explosion-induced metal spattering during laser processing, *Phys. Rev. X* 9 (2) (2019) 021052, <http://dx.doi.org/10.1103/PhysRevX.9.021052>, URL <https://link.aps.org/doi/10.1103/PhysRevX.9.021052>.
- [18] Z.A. Young, Q. Guo, N.D. Parab, C. Zhao, M. Qu, L.I. Escano, K. Fezzaa, W. Everhart, T. Sun, L. Chen, Types of spatter and their features and formation mechanisms in laser powder bed fusion additive manufacturing process, *Addit. Manuf.* 36 (2020) 101438, <http://dx.doi.org/10.1016/j.addma.2020.101438>, URL <https://linkinghub.elsevier.com/retrieve/pii/S2214860420308101>.
- [19] M. Taheri Andani, R. Dehghani, M.R. Karamooz-Ravari, R. Mirzaeifar, J. Ni, Spatter formation in selective laser melting process using multi-laser technology, *Mater. Des.* 131 (2017) 460–469, <http://dx.doi.org/10.1016/j.matdes.2017.06.040>, URL <https://linkinghub.elsevier.com/retrieve/pii/S0264127517306238>.
- [20] T. Fedina, J. Sundqvist, A.F. Kaplan, Spattering and oxidation phenomena during recycling of low alloy steel powder in Laser Powder Bed Fusion, *Mater. Today Commun.* 27 (2021) 102241, <http://dx.doi.org/10.1016/j.mtcomm.2021.102241>, URL <https://linkinghub.elsevier.com/retrieve/pii/S2352492821002336>.
- [21] M. Lutter-Günther, M. Bröker, T. Mayer, S. Lizak, C. Seidel, G. Reinhart, Spatter formation during laser beam melting of AlSi10Mg and effects on powder quality, *Procedia CIRP* 74 (2018) 33–38, <http://dx.doi.org/10.1016/j.procir.2018.08.008>, URL <https://linkinghub.elsevier.com/retrieve/pii/S2212827118307911>.
- [22] A. Gasper, B. Szost, X. Wang, D. Johns, S. Sharma, A. Clare, I. Ashcroft, Spatter and oxide formation in laser powder bed fusion of Inconel 718, *Addit. Manuf.* 24 (2018) 446–456, <http://dx.doi.org/10.1016/j.addma.2018.09.032>, URL <https://linkinghub.elsevier.com/retrieve/pii/S2214860418304524>.
- [23] J. Yin, L. Yang, X. Yang, H. Zhu, D. Wang, L. Ke, Z. Wang, G. Wang, X. Zeng, High-power laser-matter interaction during laser powder bed fusion, *Addit. Manuf.* 29 (2019) 100778, <http://dx.doi.org/10.1016/j.addma.2019.100778>, URL <https://linkinghub.elsevier.com/retrieve/pii/S2214860419303707>.
- [24] V. Gunenthiram, P. Peyre, M. Schneider, M. Dal, F. Coste, I. Koutiri, R. Fabbro, Experimental analysis of spatter generation and melt-pool behavior during the powder bed laser beam melting process, *J. Mater. Process. Technol.* 251 (2018) 376–386, <http://dx.doi.org/10.1016/j.jmatprotec.2017.08.012>, URL <https://linkinghub.elsevier.com/retrieve/pii/S0924013617303606>.
- [25] P. Bidare, I. Bitharas, R. Ward, M. Attallah, A. Moore, Fluid and particle dynamics in laser powder bed fusion, *Acta Mater.* 142 (2018) 107–120, <http://dx.doi.org/10.1016/j.actamat.2017.09.051>, URL <https://linkinghub.elsevier.com/retrieve/pii/S1359645417308170>.
- [26] M. Taheri Andani, R. Dehghani, M.R. Karamooz-Ravari, R. Mirzaeifar, J. Ni, A study on the effect of energy input on spatter particles creation during selective laser melting process, *Addit. Manuf.* 20 (2018) 33–43, <http://dx.doi.org/10.1016/j.addma.2017.12.009>, URL <https://linkinghub.elsevier.com/retrieve/pii/S2214860417304529>.
- [27] D. Wang, W. Dou, Y. Ou, Y. Yang, C. Tan, Y. Zhang, Characteristics of droplet spatter behavior and process-correlated mapping model in laser powder bed fusion, *J. Mater. Res. Technol.* 12 (2021) 1051–1064, <http://dx.doi.org/10.1016/j.jmrt.2021.02.043>, URL <https://linkinghub.elsevier.com/retrieve/pii/S2238785421001691>.
- [28] C. Pazon, B. Hoppe, T. Pichler, S. Dubiez-Le Goff, P. Forêt, T. Nguyen, E. Hryha, Reduction of incandescent spatter with helium addition to the process gas during laser powder bed fusion of Ti-6Al-4V, *CIRP J. Manuf. Sci. Technol.* 35 (2021) 371–378, <http://dx.doi.org/10.1016/j.cirpj.2021.07.004>, URL <https://linkinghub.elsevier.com/retrieve/pii/S1755581721001206>.
- [29] Q. Guo, C. Zhao, L.I. Escano, Z. Young, L. Xiong, K. Fezzaa, W. Everhart, B. Brown, T. Sun, L. Chen, Transient dynamics of powder spattering in laser powder bed fusion additive manufacturing process revealed by in-situ high-speed high-energy X-ray imaging, *Acta Mater.* 151 (2018) 169–180, <http://dx.doi.org/10.1016/j.actamat.2018.03.036>, URL <https://linkinghub.elsevier.com/retrieve/pii/S1359645418302349>.
- [30] M.J. Matthews, G. Guss, S.A. Khairallah, A.M. Rubenchik, P.J. Depond, W.E. King, Denaturation of metal powder layers in laser powder bed fusion processes, *Acta Mater.* 114 (2016) 33–42, <http://dx.doi.org/10.1016/j.actamat.2016.05.017>, URL <https://linkinghub.elsevier.com/retrieve/pii/S135964541630355X>.
- [31] X. Li, Q. Guo, L. Chen, W. Tan, Quantitative investigation of gas flow, powder-gas interaction, and powder behavior under different ambient pressure levels in laser powder bed fusion, *Int. J. Mach. Tools Manuf.* 170 (2021) 103797, <http://dx.doi.org/10.1016/j.ijmactools.2021.103797>, URL <https://linkinghub.elsevier.com/retrieve/pii/S0890695521001061>.
- [32] J. Reijnen, A. Revuelta, T. Riipinen, K. Ruusuvoori, P. Puukko, On the effect of shielding gas flow on porosity and melt pool geometry in laser powder bed fusion additive manufacturing, *Addit. Manuf.* 32 (2020) 101030, <http://dx.doi.org/10.1016/j.addma.2019.101030>, URL <https://linkinghub.elsevier.com/retrieve/pii/S2214860419312229>.
- [33] A. Ladewig, G. Schlick, M. Fisser, V. Schulze, U. Glatzel, Influence of the shielding gas flow on the removal of process by-products in the selective laser melting process, *Addit. Manuf.* 10 (2016) 1–9, <http://dx.doi.org/10.1016/j.addma.2016.01.004>, URL <https://linkinghub.elsevier.com/retrieve/pii/S2214860416300161>.
- [34] Z. Snow, L. Scime, A. Ziabari, B. Fisher, V. Paquit, Observation of spatter-induced stochastic lack-of-fusion in laser powder bed fusion using in situ process monitoring, *Addit. Manuf.* 61 (2023) 103298, <http://dx.doi.org/10.1016/j.addma.2022.103298>, URL <https://linkinghub.elsevier.com/retrieve/pii/S221486042200687X>.
- [35] C. Schwerz, A. Raza, X. Lei, L. Nyborg, E. Hryha, H. Wirdelius, In-situ detection of redeposited spatter and its influence on the formation of internal flaws in laser powder bed fusion, *Addit. Manuf.* 47 (2021) 102370, <http://dx.doi.org/10.1016/j.addma.2021.102370>, URL <https://linkinghub.elsevier.com/retrieve/pii/S2214860421005248>.
- [36] X. Zhang, B. Cheng, C. Tuffe, Simulation study of the spatter removal process and optimization design of gas flow system in laser powder bed fusion, *Addit. Manuf.* 32 (2020) 101049, <http://dx.doi.org/10.1016/j.addma.2020.101049>, URL <https://linkinghub.elsevier.com/retrieve/pii/S2214860419317749>.
- [37] F. Wirth, A. Frauchiger, K. Gutknecht, M. Cloots, Influence of the inert gas flow on the laser powder bed fusion (LPBF) process, in: C. Klahn, M. Meboldt (Eds.), *Industrializing Additive Manufacturing*, Springer International Publishing, Cham, 2021, pp. 192–204, http://dx.doi.org/10.1007/978-3-030-54334-1_14, URL https://link.springer.com/10.1007/978-3-030-54334-1_14.
- [38] A.M. Philo, C.J. Sutcliffe, S. Sillars, J. Sienz, S.G.R. Brown, N.P. Lavery, A study into the effects of gas flow inlet design of the renishaw AM250 laser powder bed fusion machine using computational modelling, in: *Proceedings of the 28th Annual International Solid Freeform Fabrication Symposium 2017: an Additive Manufacturing Conference*, University of Texas at Austin, 2017.
- [39] A.M. Philo, D. Butcher, S. Sillars, C.J. Sutcliffe, J. Sienz, S.G.R. Brown, N.P. Lavery, A multiphase CFD model for the prediction of particulate accumulation in a laser powder bed fusion process, in: L. Nastac, K. Pericleous, A.S. Sabau, L. Zhang, B.G. Thomas (Eds.), *CFD Modeling and Simulation in Materials Processing 2018*, in: *The Minerals, Metals & Materials Series*, Springer International Publishing, Cham, 2018, pp. 65–76, http://dx.doi.org/10.1007/978-3-319-72059-3_7, URL http://link.springer.com/10.1007/978-3-319-72059-3_7.
- [40] Y. Chen, G. Vastola, Y.W. Zhang, Optimization of inert gas flow inside laser powder bed fusion chamber with computational fluid dynamics, in: *Proceedings of the 29th Annual International Solid Freeform Fabrication Symposium 2018: an Additive Manufacturing Conference*, University of Texas at Austin.
- [41] A.B. Anwar, I.H. Ibrahim, Q.-C. Pham, Spatter transport by inert gas flow in selective laser melting: A simulation study, *Powder Technol.* 352 (2019) 103–116, <http://dx.doi.org/10.1016/j.powtec.2019.04.044>, URL <https://linkinghub.elsevier.com/retrieve/pii/S003259101930292X>.
- [42] J. Altmeppen, R. Nekic, P. Wagenblast, S. Staudacher, Transient simulation of particle transport and deposition in the laser powder bed fusion process: A new approach to model particle and heat ejection from the melt pool, *Addit. Manuf.* 46 (2021) 102135, <http://dx.doi.org/10.1016/j.addma.2021.102135>, URL <https://linkinghub.elsevier.com/retrieve/pii/S2214860421002992>.
- [43] C.-Y. Chien, T.-N. Le, Z.-H. Lin, Y.-L. Lo, Numerical and experimental investigation into gas flow field and spattering phenomena in laser powder bed fusion processing of Inconel 718, *Mater. Des.* 210 (2021) 110107, <http://dx.doi.org/10.1016/j.matdes.2021.110107>, URL <https://linkinghub.elsevier.com/retrieve/pii/S0264127521006626>.

- [44] J.S. Weaver, A. Schlenoff, D.C. Deisenroth, S.P. Moylan, Inert Gas Flow Speed Measurements in Laser Powder Bed Fusion Additive Manufacturing, Tech. Rep., National Institute of Standards and Technology, 2021, <http://dx.doi.org/10.6028/NIST.AMS.100-43>, URL <https://nvlpubs.nist.gov/nistpubs/ams/NIST.AMS.100-43.pdf>.
- [45] ANSYS, ANSYS Fluent Theory Guide, ANSYS Inc., 2021.
- [46] ANSYS, ANSYS Fluent User Guide, ANSYS Inc., 2021.
- [47] B.E. Poling, J.M. Prausnitz, J.P. O'Connell, *The Properties of Gases and Liquids, fifth ed.*, McGraw-Hill.
- [48] E. Strumza, O. Yehekel, S. Hayun, The effect of texture on the anisotropy of thermophysical properties of additively manufactured AISI10Mg, *Addit. Manuf.* 29 (2019) 100762, <http://dx.doi.org/10.1016/j.addma.2019.06.013>, URL <https://linkinghub.elsevier.com/retrieve/pii/S2214860419301800>.
- [49] M. Boivineau, C. Cagran, D. Doytier, V. Eyraud, M.H. Nadal, B. Wilthan, G. Pottlacher, Thermophysical properties of solid and liquid Ti-6Al-4V (TA6V) alloy, *Int. J. Thermophys.* 27 (2) (2006) 507–529, <http://dx.doi.org/10.1007/PL00021868>, URL <http://link.springer.com/10.1007/PL00021868>.
- [50] A.S. Agazhanov, D.A. Samoshkin, Y.M. Kozlovskii, Thermophysical properties of Inconel 718 alloy, *J. Phys. Conf. Ser.* 1382 (1) (2019) 012175, <http://dx.doi.org/10.1088/1742-6596/1382/1/012175>, URL <https://iopscience.iop.org/article/10.1088/1742-6596/1382/1/012175>.
- [51] E. Mendoza Jimenez, O. Ehrman, J. Beuth, B. Reeja-Jayan, Postprocessing of tungsten carbide-nickel preforms fabricated via binder jetting of sintered-agglomerated powder, *Int. J. Appl. Ceram. Technol.* (2023) ijac.14636, <http://dx.doi.org/10.1111/ijac.14636>, URL <https://ceramics.onlinelibrary.wiley.com/doi/10.1111/ijac.14636>.
- [52] E. Achenbach, Distribution of local pressure and skin friction around a circular cylinder in cross-flow up to $Re=5 \times 10^6$, *J. Fluid Mech.* 34 (4) (1968) 625–639, <http://dx.doi.org/10.1017/S0022112068002120>, URL https://www.cambridge.org/core/product/identifier/S0022112068002120/type/journal_article.
- [53] H. Schlichting, *Boundary-Layer Theory, seventh ed.*, McGraw-Hill, New York, 1979.
- [54] R.B. Bird, W.E. Stewart, E.N. Lightfoot, *Transport Phenomena, second*, Wiley international ed., J. Wiley, New York, 2002.
- [55] S.A. Morsi, A.J. Alexander, An investigation of particle trajectories in two-phase flow systems, *J. Fluid Mech.* 55 (02) (1972) 193, <http://dx.doi.org/10.1017/S0022112072001806>, URL [http://www.journals.cambridge.org/abstract_S0022112072001806](http://www.journals.cambridge.org/abstract/S0022112072001806).
- [56] R. Barati, S.A.A.S. Neyshabouri, G. Ahmadi, Development of empirical models with high accuracy for estimation of drag coefficient of flow around a smooth sphere: An evolutionary approach, *Powder Technol.* 257 (2014) 11–19, <http://dx.doi.org/10.1016/j.powtec.2014.02.045>, URL <https://linkinghub.elsevier.com/retrieve/pii/S003259101400182X>.
- [57] N.-S. Cheng, Comparison of formulas for drag coefficient and settling velocity of spherical particles, *Powder Technol.* 189 (3) (2009) 395–398, <http://dx.doi.org/10.1016/j.powtec.2008.07.006>, URL <https://linkinghub.elsevier.com/retrieve/pii/S0032591008003719>.
- [58] A. Haider, O. Levenspiel, Drag coefficient and terminal velocity of spherical and nonspherical particles, *Powder Technol.* 58 (1) (1989) 63–70, [http://dx.doi.org/10.1016/0032-5910\(89\)80008-7](http://dx.doi.org/10.1016/0032-5910(89)80008-7), URL <https://linkinghub.elsevier.com/retrieve/pii/S0032591089800087>.
- [59] J. Yin, D. Wang, H. Wei, L. Yang, L. Ke, M. Hu, W. Xiong, G. Wang, H. Zhu, X. Zeng, Dual-beam laser-matter interaction at overlap region during multi-laser powder bed fusion manufacturing, *Addit. Manuf.* 46 (2021) 102178, <http://dx.doi.org/10.1016/j.addma.2021.102178>, URL <https://linkinghub.elsevier.com/retrieve/pii/S2214860421003419>.
- [60] H. Chen, W. Yan, Spattering and denudation in laser powder bed fusion process: Multiphase flow modelling, *Acta Mater.* 196 (2020) 154–167, <http://dx.doi.org/10.1016/j.actamat.2020.06.033>, URL <https://linkinghub.elsevier.com/retrieve/pii/S1359645420304687>.
- [61] W.E. Ranz, W.R. Marshall, *Evaporation from drops: Part II*, *Chem. Eng. Prog.* 48 (1952) 173–180.
- [62] W.E. Ranz, W.R. Marshall, *Evaporation from drops: Part I*, *Chem. Eng. Prog.* 48 (1952) 141–146.
- [63] J.S. Weaver, A. Schlenoff, D. Deisenroth, S.P. Moylan, Hot-Wire Anemometer Gas Speed Measurements in a Commercial Laser Powder Bed Fusion Machine, National Institute of Standards and Technology, 2022, <http://dx.doi.org/10.18434/MDS2-2857>, URL <https://data.nist.gov/od/id/mds2-2857>. Version Number: 1.0.0 Artwork Size: 6 files, 11.3 MB Medium: application/pdf, application/x-zip-compressed, text/csv, text/plain Pages: 6 files, 11.3 MB.
- [64] L. Scime, J. Beuth, Melt pool geometry and morphology variability for the Inconel 718 alloy in a laser powder bed fusion additive manufacturing process, *Addit. Manuf.* 29 (2019) 100830, <http://dx.doi.org/10.1016/j.addma.2019.100830>, URL <https://linkinghub.elsevier.com/retrieve/pii/S2214860419306104>.
- [65] S.Z. Uddin, *Laser Powder Bed Fusion and In-Situ Monitoring of Tall Thin-Walled Structures (Ph.D. thesis)*, Carnegie Mellon University, 2022.
- [66] N. Hogasten, R. Lindner, Digital Detail Enhancement (DDE), Tech. Rep., FLIR, 2021, URL https://www.flirmedia.com/MMC/CVS/Tech_Notes/TN_0003_EN.pdf.
- [67] C. Elkins, J. Mireles, H. Estrada, D. Morgan, H. Taylor, R. Wicker, Resolving the three-dimensional flow field within commercial metal additive manufacturing machines: Application of experimental magnetic resonance velocimetry, *Addit. Manuf.* (2023) 103651, <http://dx.doi.org/10.1016/j.addma.2023.103651>, URL <https://linkinghub.elsevier.com/retrieve/pii/S2214860423002646>.
- [68] J. Shinjo, A. Kutsukake, H. Wakabayashi, K. Arakawa, A. Ogawara, H. Uchida, C. Panwisawas, R.C. Reed, In-process monitoring and direct simulation of Argon shielding gas and vapour dynamics to control laser-matter interaction in laser powder bed fusion additive manufacturing, *Addit. Manuf.* (2024) 103953, <http://dx.doi.org/10.1016/j.addma.2023.103953>, URL <https://linkinghub.elsevier.com/retrieve/pii/S2214860423005663>.
- [69] I. Bitharas, A. Burton, A. Ross, A. Moore, Visualisation and numerical analysis of laser powder bed fusion under cross-flow, *Addit. Manuf.* 37 (2021) 101690, <http://dx.doi.org/10.1016/j.addma.2020.101690>, URL <https://linkinghub.elsevier.com/retrieve/pii/S2214860420310629>.
- [70] C.T. Crowe, J.D. Schwarzkopf, M. Sommerfeld, Y. Tsuji, *Multiphase Flows with Droplets and Particles*, second ed., CRC Press, 2011, <http://dx.doi.org/10.1201/b11103>, URL <https://www.taylorfrancis.com/books/9781439840511>.
- [71] H. Shen, P. Rometsch, X. Wu, A. Huang, Influence of gas flow speed on laser plume attenuation and powder bed particle pickup in laser powder bed fusion, *JOM* 72 (3) (2020) 1039–1051, <http://dx.doi.org/10.1007/s11837-020-04020-y>, URL <http://link.springer.com/10.1007/s11837-020-04020-y>.
- [72] H. Kalman, A. Satran, D. Meir, E. Rabinovich, Pickup (critical) velocity of particles, *Powder Technol.* 160 (2) (2005) 103–113, <http://dx.doi.org/10.1016/j.powtec.2005.08.009>, URL <https://linkinghub.elsevier.com/retrieve/pii/S0032591005003694>.
- [73] Y. Shao, H. Lu, A simple expression for wind erosion threshold friction velocity, *J. Geophys. Res.* (2000).
- [74] A. Anantharaman, A. Cahyadi, K. Hadinoto, J.W. Chew, Impact of particle diameter, density and sphericity on minimum pickup velocity of binary mixtures in gas-solid pneumatic conveying, *Powder Technol.* 297 (2016) 311–319, <http://dx.doi.org/10.1016/j.powtec.2016.04.038>, URL <https://linkinghub.elsevier.com/retrieve/pii/S0032591016302066>.
- [75] J. Towns, T. Cockerill, M. Dahan, I. Foster, K. Gauthier, A. Grimshaw, V. Hazlewood, S. Lathrop, D. Lifka, G.D. Peterson, R. Roskies, J.R. Scott, N. Wilkins-Diehr, XSEDE: Accelerating scientific discovery, *Comput. Sci. Eng.* 16 (5) (2014) 62–74, <http://dx.doi.org/10.1109/MCSE.2014.80>, URL <https://ieeexplore.ieee.org/document/6866038/>.
- [76] S.T. Brown, P. Buitrago, E. Hanna, S. Sanielevici, R. Scibek, N.A. Nystrom, Bridges-2: A platform for rapidly-evolving and data intensive research, in: *Practice and Experience in Advanced Research Computing*, ACM, Boston MA USA, 2021, pp. 1–4, <http://dx.doi.org/10.1145/3437359.3465593>, URL <https://dl.acm.org/doi/10.1145/3437359.3465593>.